

Vol. 34 • No. 48 • December 1 • 2022

www.advmat.de

# ADVANCED MATERIALS

WILEY-VCH

1521-4085/2022, 48, Downloaded from https://onlinelibrary.wiley.com/doi/10.1002/adma.202208314 by University Of Hong Kong, Wiley Online Library on [07/12/2022]. See the Terms and Conditions (https://onlinelibrary.wiley.com/terms-and-conditions) on Wiley Online Library for rules of use; OA articles are governed by the applicable Creative Commons License

# 2D Transition Metal Dichalcogenide with Increased Entropy for Piezoelectric Electronics

Yulong Chen, Ziao Tian, Xiang Wang, Nian Ran, Chen Wang, Anyang Cui, Huihui Lu, Miao Zhang, Zhongying Xue, Yongfeng Mei, Paul K. Chu, Jianjun Liu, Zhigao Hu,\* and Zengfeng Di\*

Piezoelectricity in 2D transition metal dichalcogenides (TMDs) has attracted considerable interest because of their excellent flexibility and high piezoelectric coefficient compared to conventional piezoelectric bulk materials. However, the ability to regulate the piezoelectric properties is limited because the entropy is constant for certain binary TMDs other than multielement ones. Herein, in order to increase the entropy, a ternary TMDs alloy,  $\text{Mo}_{1-x}\text{W}_x\text{S}_2$ , with different W concentrations, is synthesized. The W concentration in the  $\text{Mo}_{1-x}\text{W}_x\text{S}_2$  alloy can be controlled precisely in the low-supersaturation synthesis and the entropy can be tuned accordingly. The  $\text{Mo}_{0.46}\text{W}_{0.54}\text{S}_2$  alloy ( $x = 0.54$ ) has the highest configurational entropy and best piezoelectric properties, such as a piezoelectric coefficient of  $4.22 \text{ pm V}^{-1}$  and a piezoelectric output current of 150 pA at 0.24% strain. More importantly, it can be combined into a larger package to increase the output current to 600 pA to cater to self-powered applications. Combining with excellent mechanical durability, a mechanical sensor based on the  $\text{Mo}_{0.46}\text{W}_{0.54}\text{S}_2$  alloy is demonstrated for real-time health monitoring.

in-plane direction.<sup>[1–4]</sup> When an external force is applied, the strain-induced lattice distortion gives rise to piezoelectric polarization in the materials.<sup>[5–7]</sup> Owing to the high crystallinity and ability to endure large strain, 2D-TMDs are promising candidates in applications such as sensing<sup>[8,9]</sup> and energy conversion.<sup>[10,11]</sup> Although the piezoelectric response of binary 2D-TMDs such as  $\text{MoS}_2$ ,  $\text{WS}_2$ , and  $\text{MoSe}_2$  has been improved, the ability to regulate the piezoelectric properties is still limited because piezoelectric polarization depends on the structural asymmetry.<sup>[8,12–15]</sup> For example, the piezoelectric coefficient of the sandwiched  $\text{MoS}_2$  is limited to  $2.9 \times 10^{-10} \text{ C m}^{-1}$  because the sandwiched structure with respect to the central metal atomic plane has a lower degree of structural asymmetry.<sup>[2,5]</sup>

Recently, entropy engineering has been proposed as a novel strategy to optimize the piezoelectrical<sup>[16]</sup> and thermoelectric<sup>[17]</sup> properties of materials. By increasing element species, the distortion-driven entropy, referred as configurational entropy, in a material system increases due to

## 1. Introduction

2D transition metal dichalcogenides (TMDs) are intrinsically piezoelectric due to the broken inversion symmetry along the

Y. Chen, Z. Tian, C. Wang, H. Lu, M. Zhang, Z. Xue, Z. Di  
State Key Laboratory of Functional Materials for Informatics  
Shanghai Institute of Microsystem and Information Technology  
Chinese Academy of Sciences  
Shanghai 200050, China  
E-mail: zfdi@mail.sim.ac.cn


Y. Chen, H. Lu  
Center of Materials Science and Optoelectronics Engineering  
University of Chinese Academy of Science  
Beijing 100049, China

X. Wang, A. Cui, Z. Hu  
Technical Center for Multifunctional Magneto-Optical Spectroscopy  
(Shanghai)  
Engineering Research Center of Nanophotonics & Advanced Instrument  
(Ministry of Education)  
Department of Materials  
School of Physics and Electronic Science  
East China Normal University  
Shanghai 200241, China  
E-mail: zghu@ee.ecnu.edu.cn

N. Ran, J. Liu  
State Key Laboratory of High Performance Ceramics and Superfine  
Microstructures  
Shanghai Institute of Ceramics  
Chinese Academy of Sciences  
Shanghai 200050, China

Y. Mei  
Department of Materials Science  
Fudan University  
Shanghai 200433, China

P. K. Chu  
Department of Physics  
Department of Materials Science and Engineering, and Department of  
Biomedical Engineering  
City University of Hong Kong  
Tat Chee Avenue, Kowloon, Hong Kong, China

 The ORCID identification number(s) for the author(s) of this article can be found under <https://doi.org/10.1002/adma.202201630>.

DOI: 10.1002/adma.202201630

the lattice distortion of atomic configurations.<sup>[18]</sup> Due to the increment of configurational entropy, the alloys with a high piezoelectric response could be obtained when the number of substituted components is optimized.<sup>[19–22]</sup> As a result, by doping 2D-TMDs, enhanced piezoelectricity may be realized. However, enhanced piezoelectricity has not been observed from increased entropy 2D-TMDs alloys so far and the related sensing devices have not been reported.

Herein, in order to improve the piezoelectric properties, ternary TMDs of  $\text{Mo}_{1-x}\text{W}_x\text{S}_2$  with variable W concentrations are synthesized. By adopting a solution-based precursor technique,<sup>[23]</sup> the low-supersaturation process enables precise control of the W concentration in the  $\text{Mo}_{1-x}\text{W}_x\text{S}_2$  alloy. X-ray photoelectron spectroscopy, Raman scattering, photoluminescence, and electromechanical assessment reveal that the piezoelectric coefficient of the  $\text{Mo}_{1-x}\text{W}_x\text{S}_2$  alloy is larger than those of the binary  $\text{MoS}_2$  and  $\text{WS}_2$ . Since the  $\text{Mo}_{0.46}\text{W}_{0.54}\text{S}_2$  alloy ( $x = 0.54$ ) has the similar fraction of Mo and W atoms and the highest configurational entropy, it exhibits the best piezoelectric coefficient of  $4.22 \text{ pm V}^{-1}$  among all five  $\text{Mo}_{1-x}\text{W}_x\text{S}_2$  alloys with different compositions. The output current of  $150 \text{ pA}$  at  $0.24\%$  strain is also higher than that of binary 2D materials and it can be further increased by array integration. As a result of the high piezoelectric response and

excellent mechanical durability, a mechanical sensor based on the  $\text{Mo}_{0.46}\text{W}_{0.54}\text{S}_2$  alloy is fabricated and demonstrated for real-time health monitoring.

## 2. Results and Discussion

The solution-based precursor technology is a new strategy to synthesize TMDs monolayer crystals because the supersaturation level of all the precursors can be controlled.<sup>[23]</sup> However, control of the composition is rather challenging since only one type of TMD with certain composition ratio can be obtained by optimizing the relative ratio of the amount of the precursors each time. Here, we design a low-supersaturation synthesis process to produce various TMDs alloys with controlled compositions simultaneously. In this method, a relatively low supersaturation state is produced from the vapor reactants leading to a reduced nucleation density essential for alloy growth. Moreover, the supersaturation state can be easily controlled by optimizing the distance between the precursor source and substrate, so that TMDs with diverse compositions can be fabricated. Details about the synthesis process can be found in **Figure 1a**, Experimental Section, as well as Figure S1 in the Supporting Information.

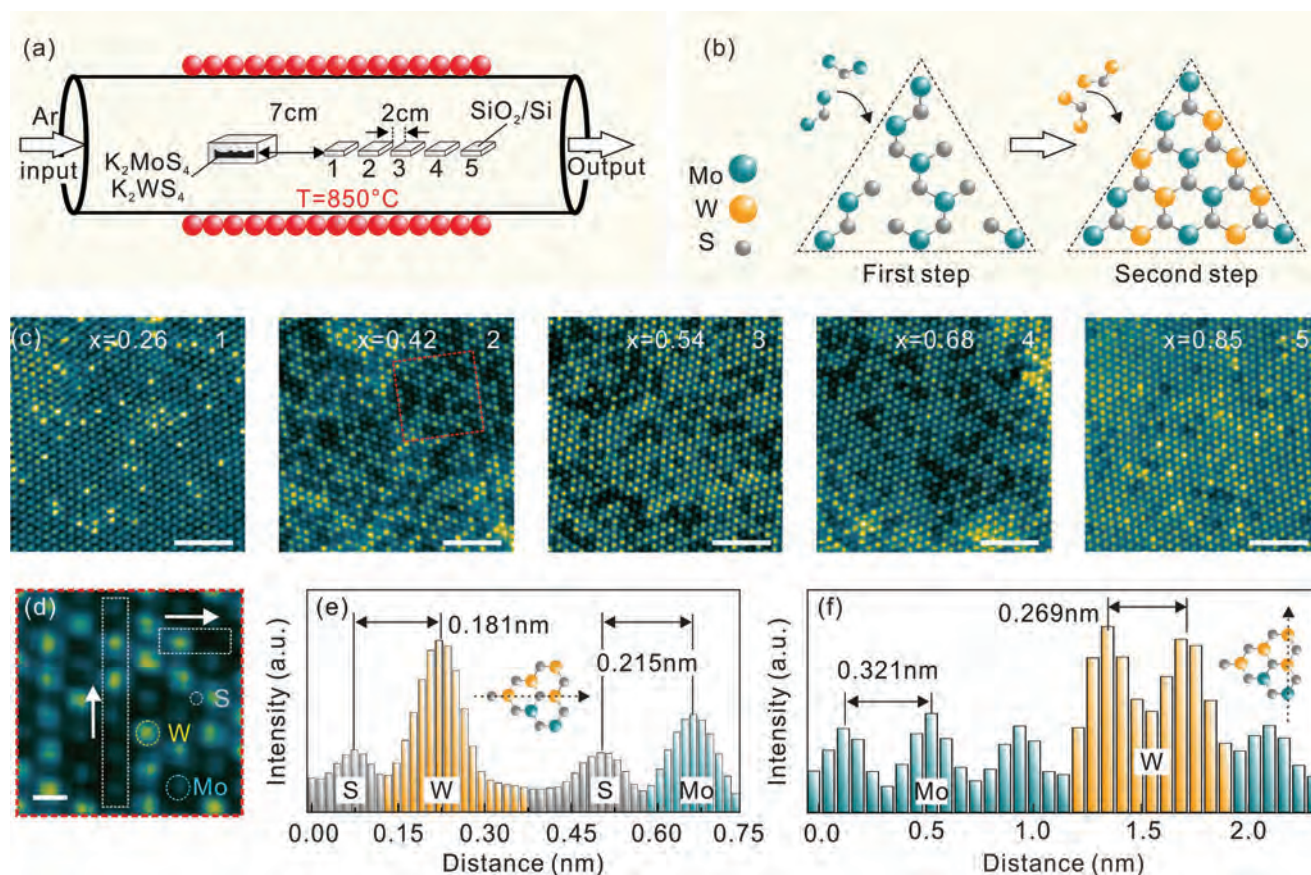


**Figure 1.** Synthesis and characterization of the monolayer  $\text{Mo}_{1-x}\text{W}_x\text{S}_2$  alloys. a) Schematic view of the low supersaturation CVD growth system consisting of five substrates with different supersaturation levels attached to the  $\text{K}_2\text{MoS}_4$  and  $\text{K}_2\text{WS}_4$  sources. b) Alloying of the  $\text{Mo}_{1-x}\text{W}_x\text{S}_2$  alloy. c) HR-TEM images of the monolayer  $\text{Mo}_{1-x}\text{W}_x\text{S}_2$  alloys (scale bar:  $2 \text{ nm}$ ). d) Magnified image of the region marked by the red square in (c-2) (scale bar:  $0.3 \text{ nm}$ ). e, f) Intensities of W, Mo, and S (e) and W and Mo (f) of the areas demarcated by the short and long white dashed lines in (d), respectively.

The  $K_2MoS_4$  and  $K_2WS_4$  precursors with a ratio of 1:1 are mixed and loaded into the CVD chamber. Five substrates are placed at different locations from the source so that the supersaturation levels can be adjusted. Owing to the lower volatilization temperature of  $K_2MoS_4$ , the sublimed S and Mo atoms are first transported downstream by the carrying gas of Ar at 750 °C to nucleation sites on the nearby substrates. According to previous reports, the distribution and density of nucleation depend on the supersaturation level.<sup>[24]</sup> In the first growth step shown in the left panel in Figure 1b, the small amount of Mo in the solution-processed precursors produces significantly lower supersaturation level and a small density of Mo-related nucleation on the substrate. The supersaturation level decreases further when the distance between the sources and substrates increases. Therefore, the nucleation density is larger on the substrate closer to the source and vice versa. In the second step (shown in the right panel in Figure 1b), the temperature increases rapidly to 850 °C.  $K_2WS_4$  vaporizes to form W-related nucleation sites which merge with the Mo nucleation sites. Because of the similar covalent lattices (138 pm for Mo and 137 pm for W) and the same crystalline structure ( $P6_3/mmc$  symmetry point group) of  $MoS_2$  and  $WS_2$ , the Mo and W atoms randomly share the metal atom sites to form the  $Mo_{1-x}W_xS_2$  alloy without clustering. Consequently, the value of  $x$  can be tuned by optimizing the distance of the substrate.

High-resolution transmission electron microscopy (HR-TEM) images are acquired from the monolayer  $Mo_{1-x}W_xS_2$  alloys synthesized at different locations in the furnace as shown in Figure 1a,c. The corresponding fast Fourier transform patterns and the deduced interplanar spacing parameters are illustrated in Figure S2 in the Supporting Information. The thickness of  $Mo_{1-x}W_xS_2$  is about 0.9 nm as determined by AFM (shown in Figure S3 in the Supporting Information) and it has a single-layer nature.<sup>[25]</sup> The single-crystal  $Mo_{1-x}W_xS_2$  with a regular triangular feature is illustrated by the HR-TEM image and the selected-area electron diffraction (SAED) pattern in Figure S4 in the Supporting Information. Due to a large difference in the atomic number between W ( $Z = 74$ ) and Mo ( $Z = 42$ ), brighter and darker spots can be resolved from the HR-TEM images, but S is not visible because of the possible inclination of the layers with respect to the direction of the incident electron beam.<sup>[20]</sup> The fraction of brighter spots corresponding to W atoms increases monotonically with larger distance between the substrate and precursor boat. The concentration of W in  $Mo_{1-x}W_xS_2$  is quantified to be  $x = 0.26$  for the closest substrate and gradually increases to  $x = 0.85$  for the farthest substrate. The  $Mo_{0.46}W_{0.54}S_2$  alloy ( $x = 0.54$ ) exhibits the highest random degree and configurational entropy.

The unequal bond lengths between S–Mo and S–W result in structural asymmetry of  $Mo_{1-x}W_xS_2$ . The atomic distribution and intensity profiles for S, Mo, and W are presented in Figure 1d–f. Figure 1d shows the magnified HR-TEM image (Figure 1c-2) of  $Mo_{0.58}W_{0.42}S_2$ . There is a clear sixfold coordination symmetry and honeycomb-like structure in which S atoms have low contrast while W and Mo atoms are yellow and blue spots, respectively. As shown in Figure 1e, the intensities of S, Mo, and W from an area surrounded by a white-dashed shorter rectangle along the white arrow in Figure 1d reveals that S atoms are immediately adjacent to Mo and W atoms with distances of

0.215 and 0.181 nm, respectively. The unequal S–Mo and S–W bond lengths break the reflection symmetry along the in-plane direction, resulting in a higher degree of asymmetry than the binary 2D-TMDs. To illustrate random substitution of Mo and W, the atomic composition of Mo and W in  $Mo_{0.58}W_{0.42}S_2$  from the white dashed longer rectangle along the white arrow in Figure 1d is shown in Figure 1f. Compared to W atoms, the number of Mo atoms is larger considering the atomic stoichiometry of the  $Mo_{0.58}W_{0.42}S_2$  alloy. The Mo–Mo distance is 0.321 nm, which is larger than that of W–W (0.269 nm). The intensity analysis suggests that the heteroatom-doping distribution of the  $Mo_{0.58}W_{0.42}S_2$  alloy is random and disordered, thus enhancing the entropy of the  $Mo_{0.58}W_{0.42}S_2$  alloy compared to pure  $MoS_2$  or  $WS_2$ .

To investigate the relationship between the atomic stoichiometry and piezoelectricity of  $Mo_{1-x}W_xS_2$  alloy, X-ray photoelectron spectroscopy (XPS), Raman scattering, PL, and electromechanical measurements are conducted, as illustrated in Figure 2. The XPS spectra of Mo 3d and W 4f of the  $Mo_{1-x}W_xS_2$  alloys with different compositions are shown in Figure 2a,b. The W 4f peak intensity increases with larger W concentration ( $x$ ) but that of the Mo 3d peak decreases or vice versa. The strong peaks at 229.5 and 232.7 eV in Figure 2a are the Mo 3d<sub>5/2</sub> and Mo 3d<sub>3/2</sub> peaks of Mo<sup>4+</sup>, respectively, and the weak peaks at 234.0 and 235.9 eV are the Mo 3d<sub>5/2</sub> and Mo 3d<sub>3/2</sub> peaks of Mo<sup>6+</sup>, respectively. The weak peaks of Mo<sup>6+</sup> are mainly due to the trace amount left from incomplete decomposition of  $K_2MoS_4$  on the substrate. As for the W 4f peaks, there are two valence states of W<sup>4+</sup> (32.8 and 35.1 eV) and W<sup>6+</sup> (37.4 and 38.5 eV) as shown in Figure 2b. Since the decomposition temperature of  $K_2WS_4$  is higher than that of  $K_2MoS_4$ , the residual hexavalent W concentration is larger accordingly. In addition, the concentration of S in the  $Mo_{1-x}W_xS_2$  alloys does not change appreciably as shown by the similar S 2p<sub>3/2</sub> and S 2p<sub>1/2</sub> peaks (Figure S5, Supporting Information). The XPS results are consistent with that provided by HR-TEM (Figure 1c).

Raman scattering spectroscopy is performed to characterize the monolayer  $Mo_{1-x}W_xS_2$  alloys as shown in Figure 2c. Prior to Raman measurement, monolayer  $Mo_{1-x}W_xS_2$  alloys pre-cleaned by deionized water to remove the possible  $K_2WS_4$  and  $K_2MoS_4$  residue during the transfer process (Figure S6, Supporting Information). In the pure monolayer  $MoS_2$ , the Raman spectrum shows the in-plane vibrational E<sub>2g</sub><sup>1</sup> (Γ) mode at 385 cm<sup>-1</sup> and an out-of-plane A<sub>1g</sub> (Γ) mode at 405 cm<sup>-1</sup>.<sup>[26]</sup> As for the pure monolayer  $WS_2$ , the strong peak at 350 cm<sup>-1</sup> is the in-plane vibration E<sub>2g</sub><sup>1</sup> (Γ) mode and the weak peak at 419 cm<sup>-1</sup> is attributed to the out-of-plane A<sub>1g</sub> (Γ) mode.<sup>[27]</sup> The positions of the E<sub>2g</sub><sup>1</sup>- $MoS_2$  and A<sub>1g</sub> peaks of the  $Mo_{1-x}W_xS_2$  alloys exhibit red and blue shifts with increasing W concentration, respectively, but the position of the E<sub>2g</sub><sup>1</sup>- $WS_2$  peak does not change. The shifts are caused by lattice distortion from substitution between W and Mo atoms and are summarized in Figure S7 in the Supporting Information.<sup>[28]</sup> In the monolayer  $Mo_{0.46}W_{0.54}S_2$  alloy, Raman mapping of three characteristic modes suggests that the distribution of Mo and W is rather uniform across the triangular flake, as shown in Figure S8 in the Supporting Information.

The PL spectra of the monolayer  $Mo_{1-x}W_xS_2$  alloys in Figure 2d show that the emission energy level is closer to that of the monolayer  $WS_2$  (631 nm, 1.98 eV) with increasing W

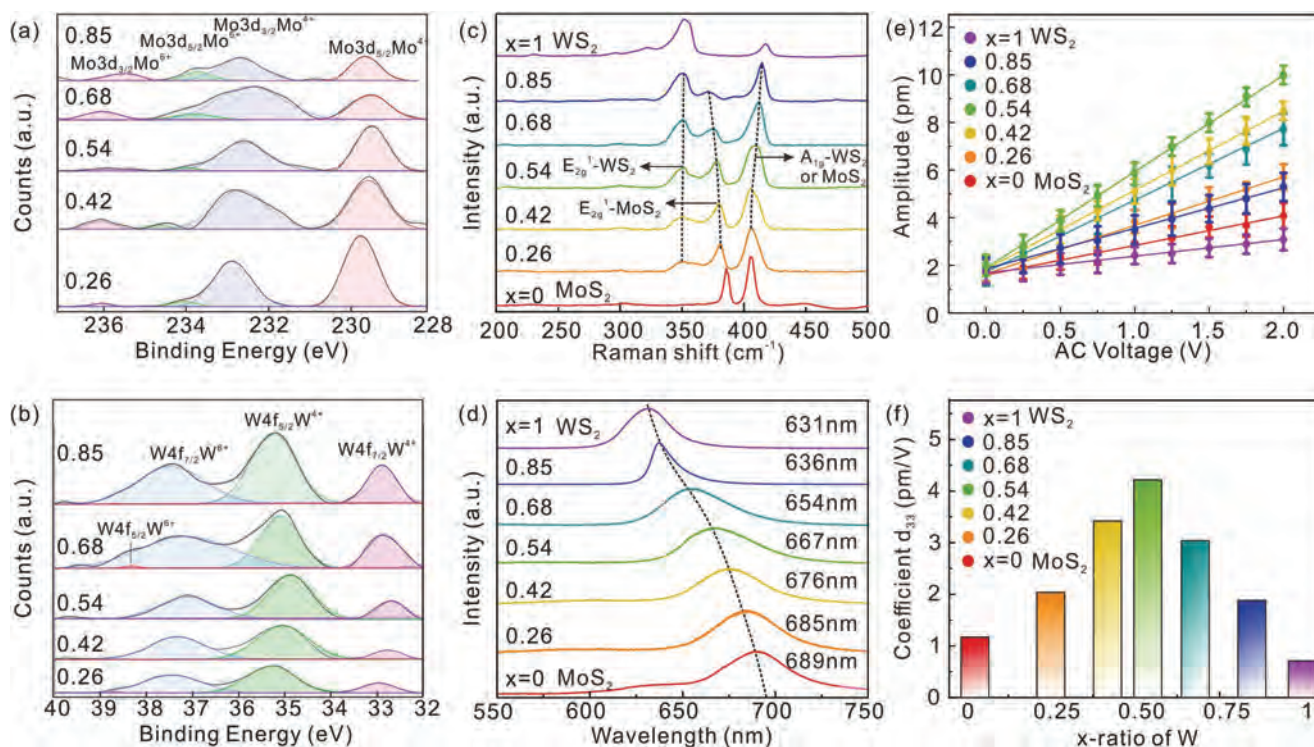


**Figure 2.** Relationship between the atomic stoichiometry and piezoelectricity of the  $\text{Mo}_{1-x}\text{W}_x\text{S}_2$  alloy. a,b) XPS spectra of Mo-3d (a) and W-4f (b) of  $\text{Mo}_{1-x}\text{W}_x\text{S}_2$  alloys with different compositions. c) Raman scattering and d) PL spectra of the monolayer  $\text{Mo}_{1-x}\text{W}_x\text{S}_2$ . e) Average piezoresponse amplitude and f) piezoresponse coefficients of the monolayer  $\text{Mo}_{1-x}\text{W}_x\text{S}_2$  samples with different compositions.

concentration and vice versa. The emission energy level is closer to that of the monolayer  $\text{MoS}_2$  (689 nm, 1.8 eV) with decreasing W concentration. The relationship between the bandgap and W concentration is illustrated in Figure S9 (Supporting Information), which is consistent with previous results.<sup>[28]</sup>

Piezoelectricity is generated by electric polarization in a non-centrosymmetric crystal structure with the symmetry broken in the lateral direction.<sup>[16,17]</sup> Owing to the structural asymmetry, a nonzero dipole moment is created in an asymmetrical order unit cell and forms a macroscopic potential difference along the lateral direction when strain is applied. This dipole moment is coupled to the materials lattice and changes in the lattice such as defects, vacancies, and doping, which can enhance electric polarization. It is expected that the piezoelectric signal from binary 2D-TMDs such as  $\text{MoS}_2$  and  $\text{WS}_2$  is weaker than that from a heteroatom-doped 2D-TMDs alloy ( $\text{Mo}_{1-x}\text{W}_x\text{S}_2$ ). In our case, though the interplanar spacing parameters for the heteroatom-doped  $\text{Mo}_{1-x}\text{W}_x\text{S}_2$  alloys with different compositions barely change (Figure S2, Supporting Information), the presence of S–Mo and S–W bonds with unequal dipole leads to a larger net dipole moment than that of the binary 2D-TMDs, thus inducing higher piezoelectric performance. Moreover, by increasing the doping-compositional space disorder, referred to as distortion-driven entropy enhancement, the heteroatom-doping-induced piezoelectric performance can be further enhanced. The preliminary density functional theory (DFT) calculation results also suggest that the entropy, especially the configurational entropy contributes to the piezoelectric effect in the  $\text{Mo}_{0.46}\text{W}_{0.54}\text{S}_2$  alloy (detail shown in Figure S10 in the

Supporting Information). As a result, the  $\text{Mo}_{0.46}\text{W}_{0.54}\text{S}_2$  alloy with  $x$  close to 0.5 (that is, almost equiatomic W and Mo) has the highest entropy and piezoelectric currents as shown in Figure S11 in the Supporting Information. The piezoelectric properties of the  $\text{Mo}_{1-x}\text{W}_x\text{S}_2$  alloys are analyzed quantitatively by piezoresponse force microscopy (PFM) as shown in Figures S12 and S13 (Supporting Information) and the variations in the PFM amplitude versus AC voltage are presented in Figures S14–S20 (Supporting Information), as summarized in Figure 2e. As expected, the maximum PFM amplitude is observed from the  $\text{Mo}_{0.46}\text{W}_{0.54}\text{S}_2$  alloy with the maximum entropy. In our quantitative analysis, the effective piezoelectric coefficient,  $d_{33}^{\text{eff}}$  of the monolayer  $\text{Mo}_{1-x}\text{W}_x\text{S}_2$  alloys is calculated using the following equation<sup>[29,30]</sup>

$$d_{33}^{\text{eff}} = \frac{A_p(\text{pm})}{V_{\text{AC}}(\text{V})} \quad (1)$$

where  $A_p(\text{pm})$  is PFM amplitude and  $V_{\text{AC}}(\text{V})$  is the amplitude of the AC voltage. The piezoresponse coefficients of monolayer  $\text{Mo}_{1-x}\text{W}_x\text{S}_2$  with different compositions can be calculated from the slope of the linearly fitted curve in Figure 2e, as summarized in Figure 2f. Because of the higher asymmetric degree in the in-plane atomic structure, the ternary  $\text{Mo}_{1-x}\text{W}_x\text{S}_2$  alloys have larger  $d_{33}^{\text{eff}}$  than both the binary  $\text{MoS}_2$  or  $\text{WS}_2$ . The monolayer  $\text{Mo}_{0.46}\text{W}_{0.54}\text{S}_2$  has the maximum  $d_{33}^{\text{eff}}$  of 4.22  $\text{pm V}^{-1}$ , while  $\text{MoS}_2$  and  $\text{WS}_2$  have the  $d_{33}^{\text{eff}}$  values of 1.25 and 0.71  $\text{pm V}^{-1}$ , respectively. All in all, XPS, Raman scattering, PL, and electromechanical evaluation reveal that the low-supersaturation

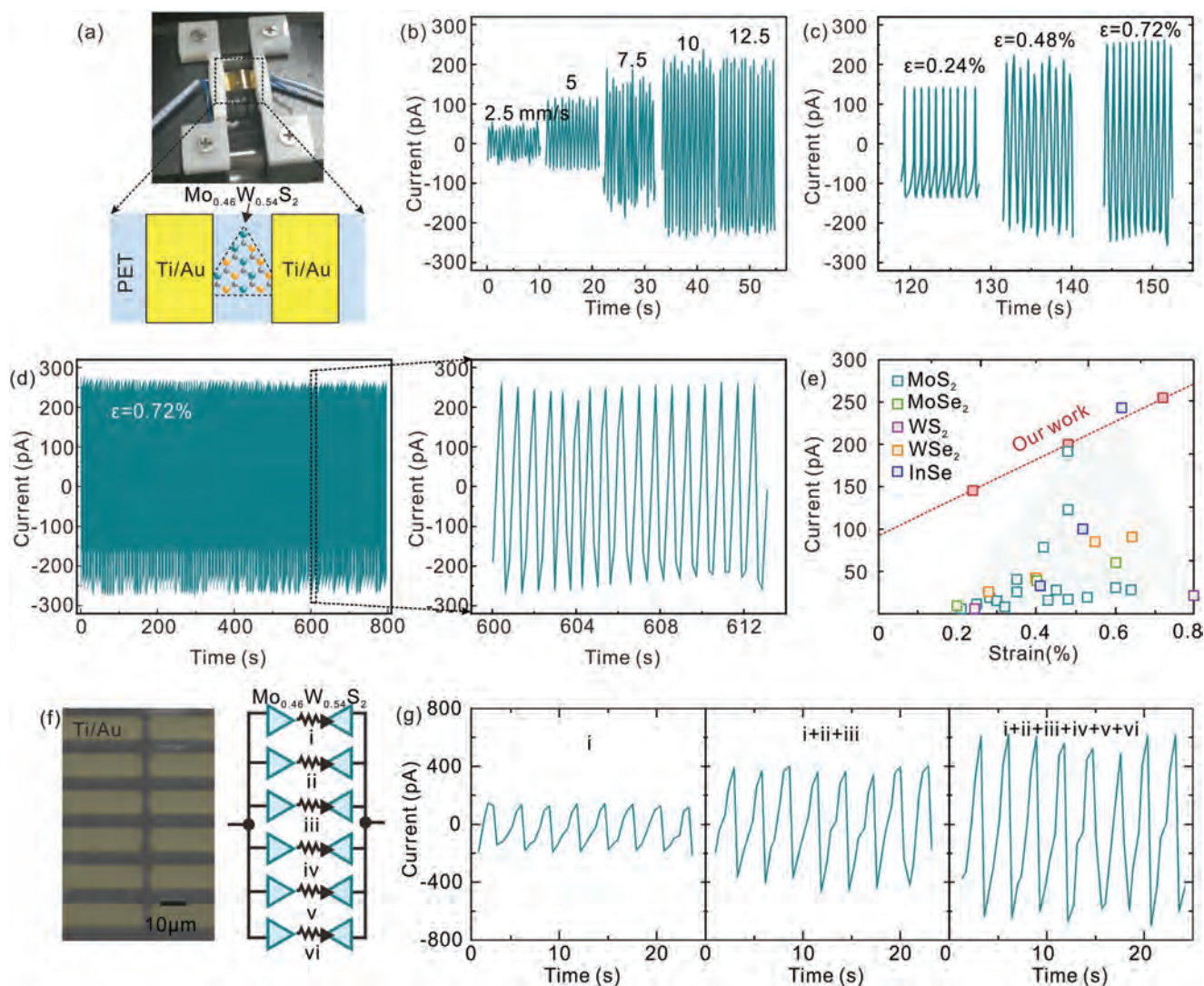


**Figure 3.** Characteristics of the piezoelectric nanogenerator based on Mo<sub>0.46</sub>W<sub>0.54</sub>S<sub>2</sub> with increased entropy (IE-PNG). a) Photograph of the mechanical loading equipment and schematic of the IE-PNG. b,c) Output currents of the IE-PNG at different strain rates (b) and strain values (c). d) Durability of the IE-PNG under cyclic loading of up to 0.72% strain at a 10 mm s<sup>-1</sup> strain rate. e) Comparison of the output currents of the binary 2D materials PNG and IE-PNG. f) SEM image of the integrated array consisting of six IE-PNGs. g) Output currents of parallel connection of one, three, and six IE-PNGs from left to right, respectively.

process is capable of tuning the elemental concentration in the 2D-TMDs flexibly and controllably. Moreover, the compositional space disorder and configurational entropy correlate with metal doping, and the piezoelectric properties can be optimized in Mo<sub>0.46</sub>W<sub>0.54</sub>S<sub>2</sub> alloy with the highest configurational entropy.

Since Mo<sub>0.46</sub>W<sub>0.54</sub>S<sub>2</sub> with increased entropy delivers the best piezoelectric performance, a piezoelectric nanogenerator (IE-PNG) is fabricated on PET, as described in Experimental Section and Figure S21 (Supporting Information) and illustrated in Figure 3a. By using this piece of equipment, the applied strain and strain rate can be programmed for periodical stretching and release of the PET substrate. The applied strain is first fixed at 0.48% to investigate the relationship between the current and strain rate. The output currents of the IE-PNG under different strain rates from 2.5 to 12.5 mm s<sup>-1</sup> are shown in Figure 3b. The output voltages of IE-PNG based on Mo<sub>0.46</sub>W<sub>0.54</sub>S<sub>2</sub> under

different load resistances or different strain rates are shown in Figure S22 in the Supporting Information. As the strain rate increases from 2.5 to 10 mm s<sup>-1</sup>, the current increases linearly from 50 to 200 pA and the linear increase is consistent with the strain-induced current equation of  $I = d_{33}EA\dot{\epsilon}$ , where  $I$  is the output current,  $d_{33}$  is the piezoelectric charge constant,  $E$  is Young's modulus,  $A$  is the cross-sectional area, and  $\dot{\epsilon}$  is the applied strain rate.<sup>[31]</sup> For certain materials,  $d_{33}$ ,  $E$ , and  $A$  are constant and a linear relationship between  $I$  and  $\dot{\epsilon}$  can be obtained. The linear relationship is observed for strain rates below 10 mm s<sup>-1</sup> and the output current is saturated when the strain rate is larger than 10 mm s<sup>-1</sup>. This phenomenon arises from layer separation between the triboelectric layer and PET substrate at the high strain rate and therefore, the generated charges cannot be derived completely. The correlation between the piezoelectric output current and the layer number of Mo<sub>1-x</sub>W<sub>x</sub>S<sub>2</sub>

is also investigated, as shown in Figure S23 in the Supporting Information. Different from two-layer binary 2D-TMDs such as  $\text{MoS}_2$ , in which the piezoelectric behavior disappears due to a symmetric cancellation of alternating orientations between the adjacent layers,<sup>[1]</sup> the two-layer  $\text{Mo}_{0.46}\text{W}_{0.54}\text{S}_2$  still exhibits a weak piezoelectric signal arising from the out-of-plane asymmetry of adjacent layers, though the intensity is attenuated considerably.

The relationship between the current and strain is investigated for a fixed strain rate of  $10 \text{ mm s}^{-1}$ , as shown in Figure 3c. The output current increases when the strain increases from 0.24% to 0.72%. According to the piezoelectric theory, the distance between the positive charge and negative charge, which correlates with the strain, determines the polarization and bound charges.<sup>[31]</sup> However, if the applied strain exceeds 0.96%, an unstable output current is observed due to significant slippage between the IE-PNG and PET substrate (see Figure S24 in the Supporting Information). The durability test results in Figure 3d indicate that the response of the IE-PNG is stable with time for cyclic loading up to 0.72% strain (more details shown in Figure S25 in the Supporting Information) at a  $10 \text{ mm s}^{-1}$  strain rate for 800 s. The output current is rather stable confirming the excellent mechanical stability. In addition, the output current is a key parameter to evaluate the performance of piezoelectric nanogenerators (PNGs), the output currents of the PNG with the binary monolayer 2D materials

and compared to those of our IE-PNG composed of the monolayer  $\text{Mo}_{0.46}\text{W}_{0.54}\text{S}_2$  alloy are shown in Figure 3e.<sup>[1,10,11,29,32–37]</sup> In our case, the output current increases linearly with the applied strain and is always higher than that of the other binary 2D materials at the similar strain state. For instance, at a low strain of 0.24%, our IE-PNG shows an output current of 150 pA that is an order of magnitude larger than those of  $\text{MoS}_2$ ,  $\text{MoSe}_2$ ,  $\text{WS}_2$ ,  $\text{WSe}_2$ , and  $\text{InSe}$ . The output current reaches 200 pA for 0.48% strain that is also higher than that of other binary 2D materials. For a strain above 0.6%, the monolayer  $\text{InSe}$ , a group-III monochalcogenide, shows a higher output current due to the largest clamped-ion piezoelectric coefficients.<sup>[38]</sup> To further improve the properties of the IE-PNG, multiple IE-PNGs can be integrated in parallel on the PET substrate to obtain an enlarged output current, as shown in Figure 3f. As expected, piezoelectric output currents with 150, 400, and 600 pA are observed from the single, triple, and sextuple IE-PNGs, respectively, when connected in parallel (Figure 3g).

Benefiting from the linear relationship between the output current and strain (shown in Figure 3e), a flexible mechanical sensor constructed with the  $\text{Mo}_{0.46}\text{W}_{0.54}\text{S}_2$  alloy is applied to monitor the human arterial pulse. The real-time arterial pulse sensor uses  $\text{Mo}_{0.46}\text{W}_{0.54}\text{S}_2$  flake (IE-APS) on the soft PDMS and the IE-APS is attached to the skin at the left wrist as schematically shown in Figure 4a. The optical microscopy image of

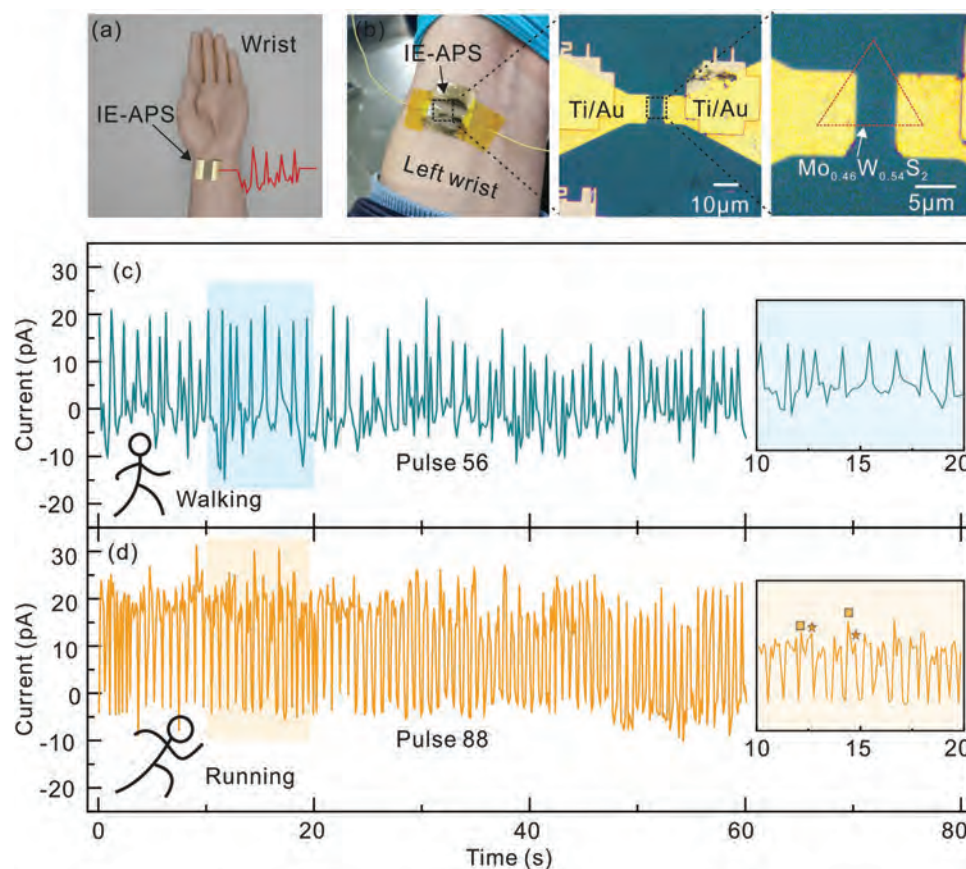


**Figure 4.** Characteristics of the real-time arterial pulse sensor based on  $\text{Mo}_{0.46}\text{W}_{0.54}\text{S}_2$  (IE-APS). a) Schematic diagram of the IE-APS placed on a human wrist. b) Optical microscopy image of the IE-APS. c,d) Output currents of two different physical modes: c) walking and d) running; the insets show the magnified pulses in the colored rectangles.

the IE-APS is shown in Figure 4b and the output currents of two different physical modes, walking and running, are presented in Figure 4c,d, respectively. The pulse rate is 56 bpm in the walking mode and increases to 88 bpm in the running mode. The peak value of the positive pulses is always slightly higher than that of the negative pulses because of the difference in the strain rates between systolic and diastolic blood pressure, implying that the time for systole is shorter than that during diastole.<sup>[39]</sup> The magnified line signals from 10 to 20 s are shown in the insets in Figure 4c,d. Compared to single peak originating from one pulse in the walking mode, two peaks denoted by square and star symbols are distinguishable in a running model, which is caused by superposition of the incoming blood wave ejected from the left ventricular and reflected wave from the lower body.<sup>[32]</sup> The capability of resolving the left ventricular and reflected wave from the incoming blood wave confirms that the IE-APS based on  $\text{Mo}_{0.46}\text{W}_{0.54}\text{S}_2$  with increased entropy has very high sensitivity in pressure detection. The fast response and high sensitivity of the self-powered mechanical sensor render it an ideal flexible device in practice.

### 3. Conclusion

Heterodoping is a feasible way to increase the structural asymmetry, compositional space disorder, and entropy of TMDs. The entropy-enhanced  $\text{Mo}_{0.46}\text{W}_{0.54}\text{S}_2$  TMD delivers exceptional piezoelectricity performance such as a piezoelectric coefficient of  $4.22 \text{ pm V}^{-1}$  and output current of 150 pA at 0.24% strain. Furthermore, it can be integrated into a larger package to increase the output current to 600 pA to cater to self-powered applications. A mechanical sensor is fabricated with the  $\text{Mo}_{0.46}\text{W}_{0.54}\text{S}_2$  TMD to monitor human arterial pulse rates in real-time for different physical modes. Owing to the high piezoelectric sensitivity, the incoming blood wave and reflected wave manifest as two peaks in the running mode. Our results demonstrate the feasibility of optimizing the properties of the piezoelectric materials for high-performance energy generators and mechanical sensors by increasing the entropy of the alloy, and the novel strategy has large potential pertaining to the design of next-generation piezoelectric materials and self-powered wearable devices.

### 4. Experimental Section

**Sample Preparation:**  $\text{K}_2\text{MoS}_4$  and  $\text{K}_2\text{WS}_4$  synthesized from  $(\text{NH}_4)_2\text{MoS}_4$  powder (99.9%, Sigma Aldrich) and  $(\text{NH}_4)_2\text{WS}_4$  powder (99.9%, Sigma Aldrich)<sup>[40]</sup> were used as precursors in CVD using a movable single heating furnace. A quartz boat loaded with  $\text{K}_2\text{MoS}_4$  and  $\text{K}_2\text{WS}_4$  with a molar mass ratio of 1:1 was placed in a 2-inch quartz tube. The 300 nm  $\text{SiO}_2/\text{Si}$  ( $1 \times 1 \text{ cm}$ ) substrate was cleaned with acetone and methanol. The composition of the  $\text{Mo}_{1-x}\text{W}_x\text{S}_2$  alloys was controlled by varying the loading distance between the substrate and precursor boat. Before synthesis, the tube was evacuated to a pressure of 1 Pa and then filled with Ar gas to atmospheric pressure. The furnace put far away from the precursors was heated to  $850 \text{ }^\circ\text{C}$  for 60 min under 200 sccm Ar flow. Afterwards, the furnace was pushed to the precursors and maintained 10 min for the synthesis. The temperature of the precursors increased rapidly from room temperature to  $850 \text{ }^\circ\text{C}$  and after the synthesis, the

furnace was immediately pushed away from the precursor and the Ar flow rate was adjusted to 500 sccm to enable cooling.

**PFM Characterization:** The surface morphology of the monolayer alloys was examined on a commercial AFM system (Dimension Icon, Bruker) and the PFM mode was employed to detect the piezoelectricity with the aid of a conductive “SCM-PIT” tip coated by Pt/Ir. To avoid contact resonance at the tip-sample junction, the frequency of the applied AC voltage was 15 kHz which was far away from the contact resonance frequency (above 120 kHz).

**HR-TEM Characterization:** The atomic structure and crystallinity of the monolayer  $\text{Mo}_{1-x}\text{W}_x\text{S}_2$  samples were characterized by HR-TEM (JEOL, JEM-ARM 300F) at 80 kV.

**XPS Characterization:** The elemental composition of the  $\text{Mo}_{1-x}\text{W}_x\text{S}_2$  alloys was determined by X-ray photoelectron spectroscopy (Kratos AXIS Supra XPS equipped with a monochromatic Al  $K_{\alpha}$  source) referenced to the C1s peak at 284.8 eV.

**PL and Raman Scattering Characterization:** Photoluminescence and Raman scattering were conducted on the HORIBA Jobin Yvon HR800 with a 514 nm semiconductor laser with a spot size of  $1 \mu\text{m}$  in air under ambient conditions. High-resolution Raman mapping was performed using the confocal  $\mu\text{-PL}$  system (WITec, alpha-300) with a 532 nm wavelength laser and  $100\times$  (0.9 NA) objective lens. The grating was  $1800 \text{ g mm}^{-1}$ .

**Electrical Output Characterization:** The low-noise output currents of the monolayer  $\text{Mo}_{1-x}\text{W}_x\text{S}_2$  IE-PNGs were measured on a picoammeter (Keithley, 4200) and a bending machine was utilized to generate the programmed driving strain between the two electrodes.

**On-Body Experiments:** The left wrist of the volunteer (one of the authors of this paper) was cleaned with soap and water, and dried. The real-time arterial pulse sensor was attached onto the volunteer skin to monitor the actual pulses. The volunteer involved in this context gave written, fully informed consent before participation in the study. The experiments conducted in this study were not subject to ethical approval.

### Supporting Information

Supporting Information is available from the Wiley Online Library or from the author.

### Acknowledgements

Y.C., Z.T., and X.W. contributed equally to this work. This work was supported by National Natural Science Foundation of China (51925208, 61974157, 62122082), Key Research Project of Frontier Science, Chinese Academy of Sciences (QYZDB-SSW-JSC021), National Science and Technology Major Project (2016ZX02301003), Science and Technology Innovation Action Plan of Shanghai Science and Technology Committee (20501130700), Strategic Priority Research Program (B) of the Chinese Academy of Sciences (XDB30030000), Key Research Program of the Chinese Academy of Sciences (XDPB22), Science and Technology Commission of Shanghai Municipality (19JC1415500, 21JC1406100), and Shenzhen – Hong Kong Innovative Collaborative Research and Development Program (SGLH20181109110802117 and CityU 9240014).

### Conflict of Interest

The authors declare no conflict of interest.

### Data Availability Statement

The data that support the findings of this study are available from the corresponding author upon reasonable request.



## Keywords

2D alloys, entropy, nanogenerators, piezoelectricity, sensors

Received: February 19, 2022

Revised: May 15, 2022

Published online: June 13, 2022

- [1] W. Wu, L. Wang, Y. Li, F. Zhang, L. Lin, S. Niu, D. Chenet, X. Zhang, Y. Hao, T. F. Heinz, J. Hone, Z. L. Wang, *Nature* **2014**, *514*, 470.
- [2] H. Zhu, Y. Wang, J. Xiao, M. Liu, S. Xiong, Z. J. Wong, Z. Ye, Y. Ye, X. Yin, X. Zhang, *Nat. Nanotechnol.* **2015**, *10*, 151.
- [3] K.-A. N. Duerloo, M. T. Ong, E. J. Reed, *J. Phys. Chem. Lett.* **2012**, *3*, 2871.
- [4] K. H. Michel, B. Verberck, *Phys. Rev. B* **2011**, *83*, 115328.
- [5] S. A. Han, J. Lee, J. J. Lin, S. W. Kim, J. H. Kim, *Nano Energy* **2019**, *57*, 680.
- [6] Y. Y. Peng, M. L. Que, J. Tao, X. D. Wang, J. F. Lu, G. F. Hu, B. S. Wan, Q. Xu, C. F. Pan, *2D Mater.* **2018**, *5*, 042003.
- [7] L. Wang, S. Liu, X. Feng, C. Zhang, L. Zhu, J. Zhai, Y. Qin, Z. L. Wang, *Nat. Nanotechnol.* **2020**, *15*, 661.
- [8] W. B. Choi, J. Y. Kim, E. H. Lee, G. Mehta, V. Prasad, *ACS Appl. Mater. Interfaces* **2021**, *13*, 13596.
- [9] M. J. Dai, W. Zheng, X. Zhang, S. M. Wang, J. H. Lin, K. Li, Y. X. Hu, E. W. Sun, Y. F. Qiu, Y. Q. Fu, W. W. Cao, P. A. Hu, *Nano Lett.* **2020**, *20*, 201.
- [10] S. A. Han, T. H. Kim, S. K. Kim, K. H. Lee, H. J. Park, J. H. Lee, S. W. Kim, *Adv. Mater.* **2018**, *30*, 1870143.
- [11] J. H. Lee, J. Y. Park, E. B. Cho, T. Y. Kim, S. A. Han, T. H. Kim, Y. Liu, S. K. Kim, C. J. Roh, H. J. Yoon, H. Ryu, W. Seung, J. S. Lee, J. Lee, S. W. Kim, *Adv. Mater.* **2017**, *29*, 1606667.
- [12] F. Li, T. Shen, C. Wang, Y. P. Zhang, J. J. Qi, H. Zhang, *Nano-Micro Lett.* **2020**, *12*, 106.
- [13] L. Dong, J. Lou, V. B. Shenoy, *ACS Nano* **2017**, *11*, 8242.
- [14] L. Qi, S. C. Ruan, Y. J. Zeng, *Adv. Mater.* **2021**, *33*, 2100347.
- [15] R. X. Fei, W. B. Li, J. Li, L. Yang, *Appl. Phys. Lett.* **2015**, *107*, 173104.
- [16] Y. W. Chen, J. J. Ruan, J. M. Ting, Y. H. Su, K. S. Chang, *Ceram. Int.* **2021**, *47*, 11451.
- [17] R. Liu, H. Chen, K. Zhao, Y. Qin, B. Jiang, T. Zhang, G. Sha, X. Shi, C. Uher, W. Zhang, L. Chen, *Adv. Mater.* **2017**, *29*, 1702712.
- [18] J. W. Yeh, W. K. Chen, S. J. Lin, J. Y. Gan, T. S. Chin, T. T. Shun, C. H. Tsau, S. Y. Chang, *Adv. Energy Mater.* **2004**, *6*, 299.
- [19] F. Tasnádi, B. Alling, C. Hoglund, G. Wingqvist, J. Birch, L. Hultman, I. A. Abrikosov, *Phys. Rev. Lett.* **2010**, *104*, 137601.
- [20] K. Datta, R. B. Neder, J. Chen, J. C. Neufeind, B. Mihailova, *Phys. Rev. Lett.* **2017**, *119*, 207604.
- [21] K. R. Talley, S. L. Millican, J. Mangum, S. Siol, C. B. Musgrave, B. Gorman, A. M. Holder, A. Zakutayev, G. L. Brenneka, *Phys. Rev. Mater.* **2018**, *2*, 063802.
- [22] X. Li, J. Ma, K. Chen, C. Li, X. Zhang, L. An, *Ceram. Int.* **2022**, *48*, 12848.
- [23] J. Lee, S. Pak, Y. W. Lee, Y. Park, A. R. Jang, J. Hong, Y. Cho, B. Hou, S. Lee, H. Y. Jeong, H. S. Shin, S. M. Morris, S. Cha, J. I. Sohn, J. M. Kim, *ACS Nano* **2019**, *13*, 13047.
- [24] J. Lee, S. Pak, P. Giraud, Y. W. Lee, Y. Cho, J. Hong, A. R. Jang, H. S. Chung, W. K. Hong, H. Y. Jeong, H. S. Shin, L. G. Occhipinti, S. M. Morris, S. Cha, J. I. Sohn, J. M. Kim, *Adv. Mater.* **2017**, *29*, 1702206.
- [25] C. L. Tan, W. Zhao, A. Chaturvedi, Z. Fei, Z. Y. Zeng, J. Z. Chen, Y. Huang, P. Ercius, Z. M. Luo, X. Y. Qi, B. Chen, Z. C. Lai, B. Li, X. Zhang, J. Yang, Y. Zong, C. H. Jin, H. M. Zheng, C. Kloc, H. Zhang, *Small* **2016**, *12*, 1866.
- [26] H. Li, Q. Zhang, C. C. R. Yap, B. K. Tay, T. H. T. Edwin, A. Olivier, D. Baillargeat, *Adv. Funct. Mater.* **2012**, *22*, 1385.
- [27] C. X. Cong, J. Z. Shang, X. Wu, B. C. Cao, N. Peimyo, C. Qiu, L. T. Sun, T. Yu, *Adv. Opt. Mater.* **2014**, *2*, 131.
- [28] J. Park, M. S. Kim, B. Park, S. H. Oh, S. Roy, J. Kim, W. Choi, *ACS Nano* **2018**, *12*, 6301.
- [29] S. K. Kim, R. Bhatia, T. H. Kim, D. Seol, J. H. Kim, H. Kim, W. Seung, Y. Kim, Y. H. Lee, S. W. Kim, *Nano Energy* **2016**, *22*, 483.
- [30] X. Wang, A. Cui, F. Chen, L. Xu, Z. Hu, K. Jiang, L. Shang, J. Chu, *Small* **2019**, *15*, 1903106.
- [31] J. Sirohi, I. Chopra, *J. Intell. Mater. Syst. Struct.* **2000**, *11*, 246.
- [32] M. Dai, Z. Wang, F. Wang, Y. Qiu, J. Zhang, C. Y. Xu, T. Zhai, W. Cao, Y. Fu, D. Jia, Y. Zhou, P. A. Hu, *Nano Lett.* **2019**, *19*, 5410.
- [33] L. Li, P. Wen, Y. Yang, N. Huo, J. Li, *J. Mater. Chem. C* **2021**, *9*, 1396.
- [34] F. Xue, J. Zhang, W. Hu, W. T. Hsu, A. Han, S. F. Leung, J. K. Huang, Y. Wan, S. Liu, J. Zhang, J. H. He, W. H. Chang, Z. L. Wang, X. Zhang, L. J. Li, *ACS Nano* **2018**, *12*, 4976.
- [35] P.-K. Yang, S.-A. Chou, C.-H. Hsu, R. J. Mathew, K.-H. Chiang, J.-Y. Yang, Y.-T. Chen, *Nano Energy* **2020**, *75*, 104879.
- [36] P. Li, Z. Zhang, *ACS Appl. Mater. Interfaces* **2020**, *12*, 58132.
- [37] H. Khan, N. Mahmood, A. Zavabeti, A. Elbourne, M. A. Rahman, B. Y. Zhang, V. Krishnamurthi, P. Atkin, M. B. Ghasemian, J. Yang, G. Zheng, A. R. Ravindran, S. Walia, L. Wang, S. P. Russo, T. Daeneke, Y. Li, K. Kalantar-Zadeh, *Nat. Commun.* **2020**, *11*, 3449.
- [38] W. B. Li, J. Li, *Nano Res.* **2015**, *8*, 3796.
- [39] D. Shier, J. Butler, R. Lewis, *Human Anatomy & Physiology*, McGraw Hill, Boston, MA, USA **2001**.
- [40] A. Cordovan, P. Blanchard, C. Lancelot, G. Frey, C. Lamonier, *ACS Catal.* **2015**, *5*, 2966.

# ADVANCED MATERIALS

## Supporting Information

for *Adv. Mater.*, DOI: 10.1002/adma.202201630

2D Transition Metal Dichalcogenide with Increased  
Entropy for Piezoelectric Electronics

*Yulong Chen, Ziao Tian, Xiang Wang, Nian Ran, Chen Wang, Anyang Cui, Huihui Lu, Miao Zhang, Zhongying Xue, Yongfeng Mei, Paul K. Chu, Jianjun Liu, Zhigao Hu,\* and Zengfeng Di\**

# Supporting Information

## 2D Transition Metal Dichalcogenide with Increased Entropy for Piezoelectric Electronics

*Yulong Chen, Ziao Tian, Xiang Wang, Nian Ran, Chen Wang, Anyang Cui, Huihui Lu,  
Miao Zhang, Zhongying Xue, Yongfeng Mei, Paul K. Chu, Jianjun Liu, Zhigao Hu\*  
and Zengfeng Di\**

Dr. Y. Chen, Prof. Z. Tian, Prof. C. Wang, Dr. H. Lu, Prof. M. Zhang, Prof. Z. Xue, Prof.  
Z. Di

State Key Laboratory of Functional Materials for Informatics, Shanghai Institute of  
Microsystem and Information Technology, Chinese Academy of Sciences, Shanghai  
200050, China

E-mail: [zfdi@mail.sim.ac.cn](mailto:zfdi@mail.sim.ac.cn) (Z. F. Di)

Dr. X. Wang, Dr. A. Cui, Prof Z. Hu,

Technical Center for Multifunctional Magneto-Optical Spectroscopy (Shanghai),  
Engineering Research Center of Nanophotonics &Advanced Instrument (Ministry of  
Education), Department of Materials, School of Physics and Electronic Science, East  
China Normal University, Shanghai 200241, China

E-mail: [zghu@ee.ecnu.edu.cn](mailto:zghu@ee.ecnu.edu.cn) (Z. G. Hu)

Dr. N. Ran, Prof. J. Liu

State Key Laboratory of High Performance Ceramics and Superfine Microstructures,  
Shanghai Institute of Ceramics, Chinese Academy of Sciences, Shanghai 200050,  
China

Prof. Y. Mei

Department of Materials Science, Fudan University, Shanghai 200433, China

Prof. P. K. Chu

Department of Physics, Department of Materials Science and Engineering, and  
Department of Biomedical Engineering, City University of Hong Kong, Tat Chee  
Avenue, Kowloon, Hong Kong, China

Dr. Y. Chen, Dr. H. Lu

Center of Materials Science and Optoelectronics Engineering, University of Chinese  
Academy of Science, Beijing 100049, China

**Keywords:** Entropy; 2D alloys; piezoelectricity; nanogenerators; sensors

## Synthesis

The locations of the precursors and substrates in the single furnace are schematically shown in Figure S1. The tube was flushed with Ar three times and then filled with Ar gas. It was heated to 850 °C in 60 min under Ar at a flow rate of 200 sccm (Position 1). After that, the furnace was pushed to the precursors and the position was maintained for 10 minutes to carry out the synthesis (Position 2). Afterwards, the furnace was pulled away rapidly from the precursor and the Ar flow rate was adjusted to 500 sccm during cooling.

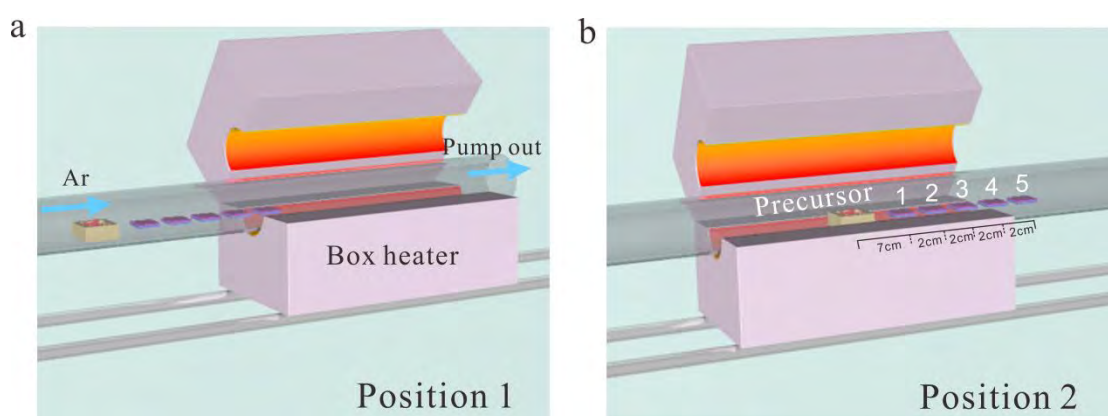


**Figure S1.** Schematic of the APCVD system: (a) Before synthesis, the furnace was placed far away from the precursor to avoid thermal radiation; (b) During synthesis, the furnace was moved to the precursors for 10 minutes.

### **Fast Fourire transform patterns**

Figure S2(a) shows the fast Fourier transform (FFT) patterns that are converted from HR-TEM images displayed in Figure 1(c) in the main text. It reveals monolayer  $\text{Mo}_{1-x}\text{W}_x\text{S}_2$  alloys with different compositions have similar FFT patterns as that of monolayer  $\text{MoS}_2$  which can be indexed as 2H- $\text{MoS}_2$  along [001] zone axis characterized by sixfold symmetry.<sup>1</sup> Two of the spots nearest to the center can be indexed as (100) and (010) lattice planes<sup>2</sup> and the corresponding lattice planes in real space are shown in Figure S2(b) by dashed blue and red lines.<sup>3</sup> The interplanar spacings of  $\text{Mo}_{1-x}\text{W}_x\text{S}_2$  corresponded to the (100) and (010) lattice planes with various concentrations of W in  $\text{Mo}_{1-x}\text{W}_x\text{S}_2$  ( $x$ ) are summarized in Figure S2(c). It is found that the measured (100) and (010) interplanar spacings fluctuate slightly ranging from 0.263 nm to 0.276 nm, which are consistent with references.<sup>4-6</sup> The (100) interplanar spacings are 0.276 nm, 0.276 nm, 0.275 nm, 0.274 nm, and 0.275nm as the concentrations of W in  $\text{Mo}_{1-x}\text{W}_x\text{S}_2$ ,  $x$ , are 0.26, 0.42, 0.54, 0.68, and 0.85, respectively. Therefore, the values of (100) interplanar spacings for monolayer  $\text{Mo}_{1-x}\text{W}_x\text{S}_2$  alloys always stay constant regardless of  $x$ . The similar trend is also found in (010) interplanar spacings. So, the lattice parameters are unchanged as W concentration in  $\text{Mo}_{1-x}\text{W}_x\text{S}_2$  varies, and the change of piezoelectric constant should be related to the varying of configurational entropy.

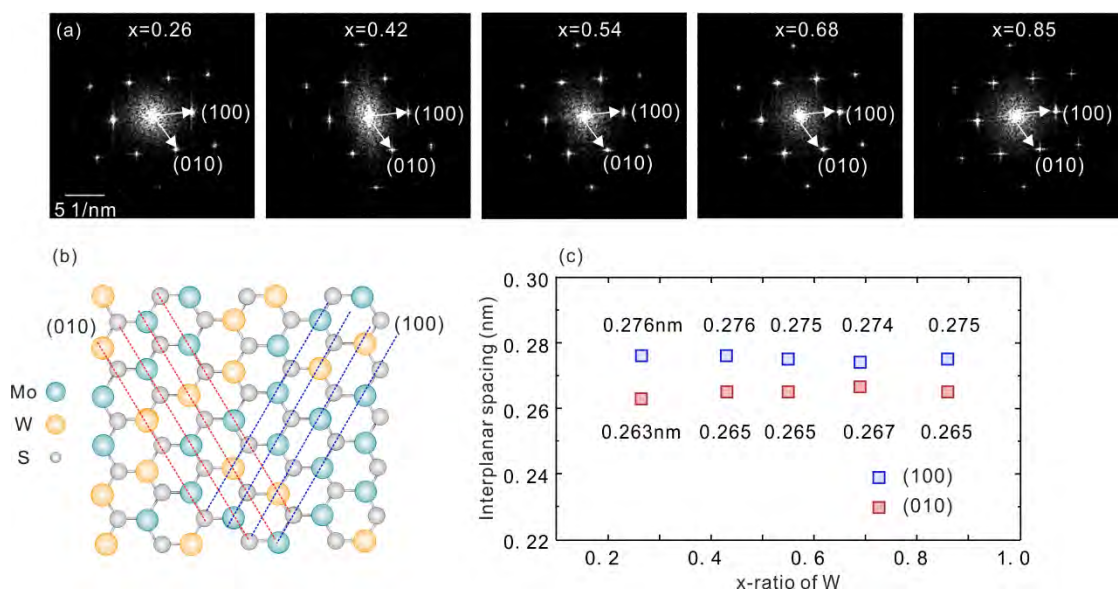


**Figure S2.** (a) The fast Fourier transform (FFT) patterns of Mo<sub>1-x</sub>W<sub>x</sub>S<sub>2</sub> alloys with various concentrations. (b) Schematic drawing of the top view of Mo<sub>1-x</sub>W<sub>x</sub>S<sub>2</sub> alloys in real space. Dashed red and blue lines represent the (010) and (100) lattice planes, respectively. (c) The parameters of interplanar spacing for Mo<sub>1-x</sub>W<sub>x</sub>S<sub>2</sub> alloys with various concentrations.

### **Film thickness measurement**

The thickness of the Mo<sub>1-x</sub>W<sub>x</sub>S<sub>2</sub> nanosheet sample was measured by AFM, and it was found to be approximately 0.9 nm, suggesting a monolayer structure.

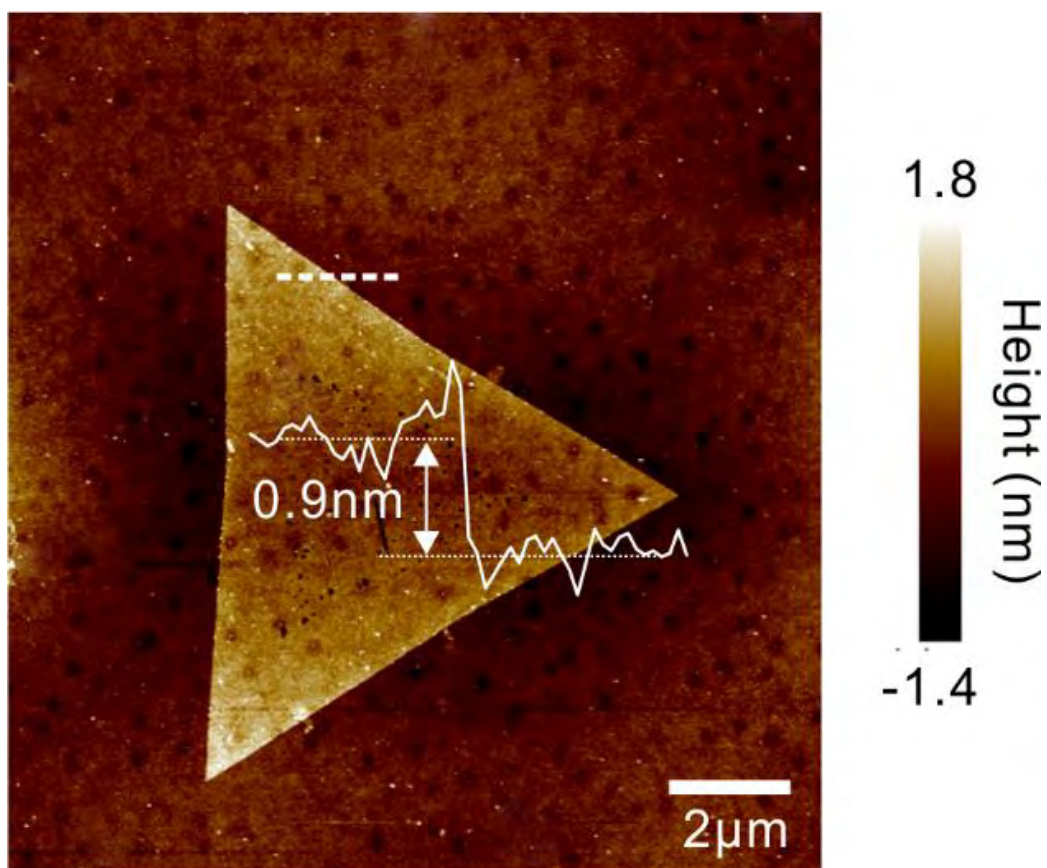


**Figure S3.** AFM height image of the monolayer Mo<sub>1-x</sub>W<sub>x</sub>S<sub>2</sub>. The line scans along the white dashed line is shown as the solid white curve.

### **Characterization by HR-TEM**

The triangular monolayer film was laid on the Cu TEM elliptical grid as shown by the white dashed line in Figure S4. The indexed selected-area electron diffraction (SAED) pattern in the inset in Figure S4 reveals a perfect hexagonal single-crystal lattice.



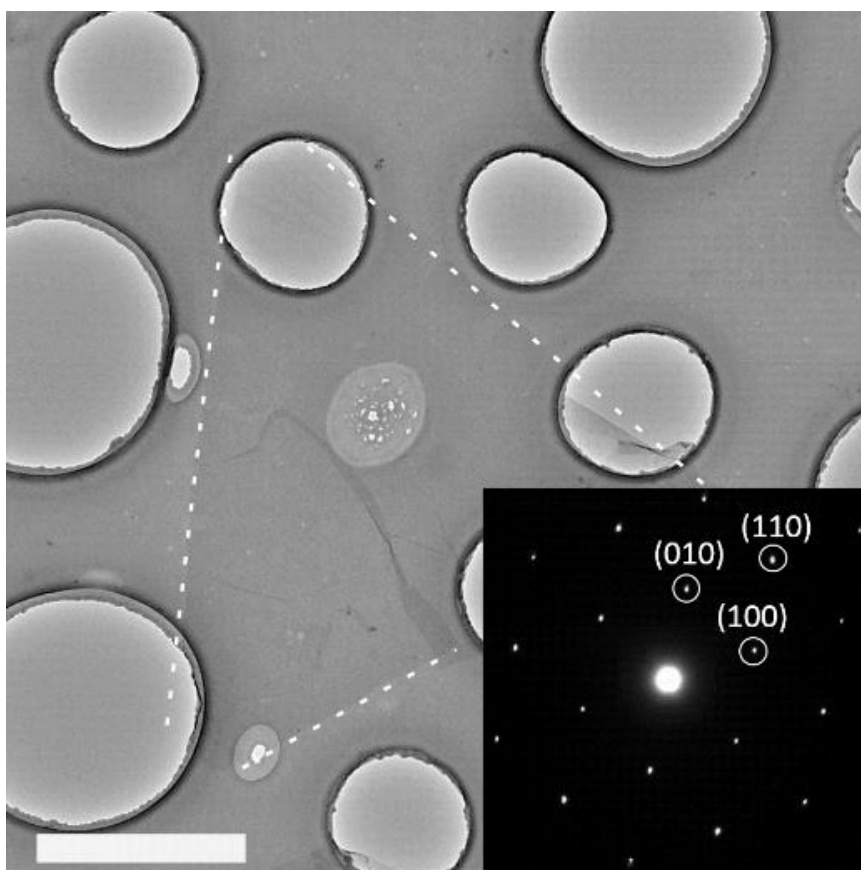


**Figure S4.** Low-magnification TEM image of the Mo<sub>1-x</sub>W<sub>x</sub>S<sub>2</sub> alloy (x = 0.42) on the Cu grid (Scale bar: 2  $\mu$ m) with the SAED patterns shown in the inset.

## XPS S 2p peaks

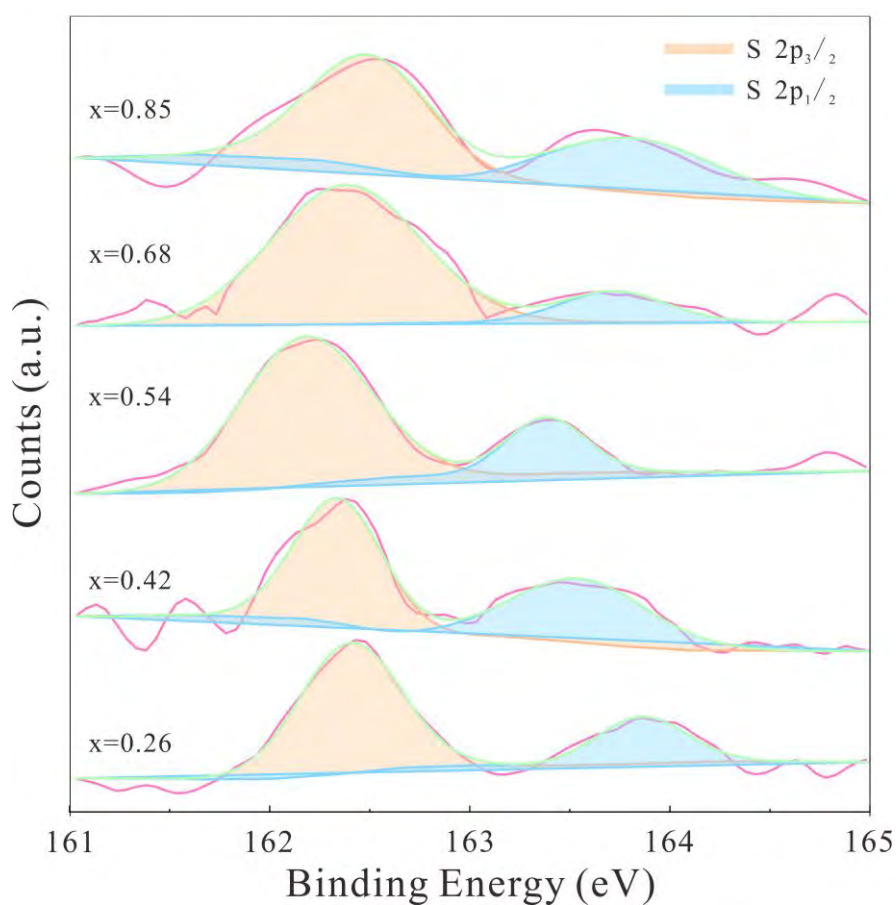


**Figure S5.** XPS spectra showing the binding energies of the S 2p peaks in the Mo<sub>1-x</sub>W<sub>x</sub>S<sub>2</sub> alloys with different compositions.

## Raman spectra of residual K<sub>2</sub>WS<sub>4</sub> and K<sub>2</sub>MoS<sub>4</sub>

The Raman spectra of the precursors (K<sub>2</sub>WS<sub>4</sub>, K<sub>2</sub>MoS<sub>4</sub>) and the monolayer Mo<sub>1-x</sub>W<sub>x</sub>S<sub>2</sub> samples with different compositions are shown in Figure S6. In the case of K<sub>2</sub>WS<sub>4</sub> and K<sub>2</sub>MoS<sub>4</sub>, the peaks at 456, 462, 474 and 487 cm<sup>-1</sup> are associated with the  $\nu$  (W-S) vibration of the WS<sub>4</sub><sup>2-</sup> anion, and the peaks at 454, 465, 472 and 482 cm<sup>-1</sup> are

related to the  $\nu$  (Mo-S) vibration of the  $\text{MoS}_4^{2-}$  anion.<sup>7,8</sup> In the  $\text{Mo}_{1-x}\text{W}_x\text{S}_2$  case, these peaks are barely observed regardless of the value of  $x$  (the peak at  $520\text{ cm}^{-1}$  is attributed to Si substrates), implying that the amounts  $\text{K}_2\text{WS}_4$  and  $\text{K}_2\text{MoS}_4$  residual in the alloy samples are below the detection limit. Since  $\text{K}_2\text{WS}_4$  and  $\text{K}_2\text{MoS}_4$  are both water dissolvable, prior to Raman measurement, the as-grown  $\text{Mo}_{1-x}\text{W}_x\text{S}_2$  is pre-cleaned by deionized water to remove the possible  $\text{K}_2\text{WS}_4$  and  $\text{K}_2\text{MoS}_4$  residue during the transfer process as reported previously.<sup>9</sup>

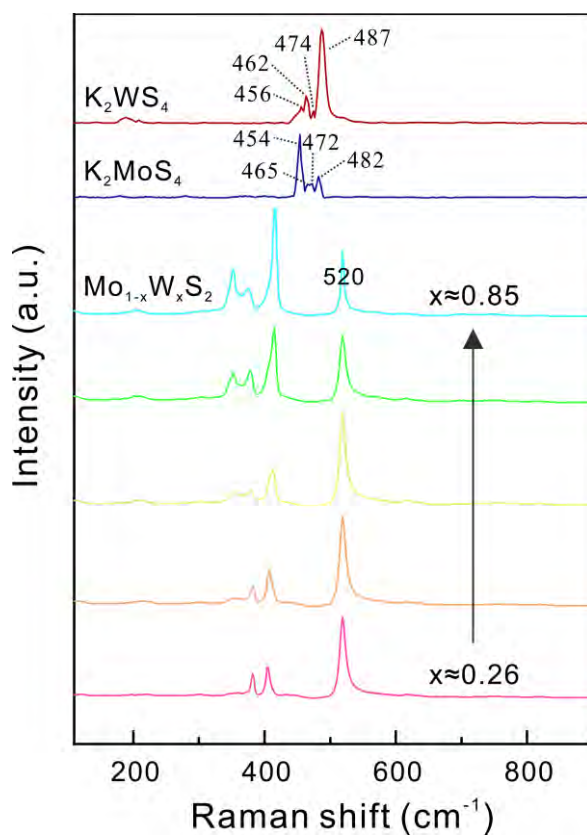


**Figure S6.** Raman spectra of two precursors ( $\text{K}_2\text{WS}_4$ ,  $\text{K}_2\text{MoS}_4$ ) and the monolayer  $\text{Mo}_{1-x}\text{W}_x\text{S}_2$  samples with different compositions.

## Raman scattering

A larger W concentration results in red and blue shifts of the Raman  $E_{2g}^1$ -MoS<sub>2</sub> and  $A_{1g}$  peaks, respectively. But, the position of the  $E_{2g}^1$ -WS<sub>2</sub> peaks of the monolayer Mo<sub>1-x</sub>W<sub>x</sub>S<sub>2</sub> alloys is nearly the same.

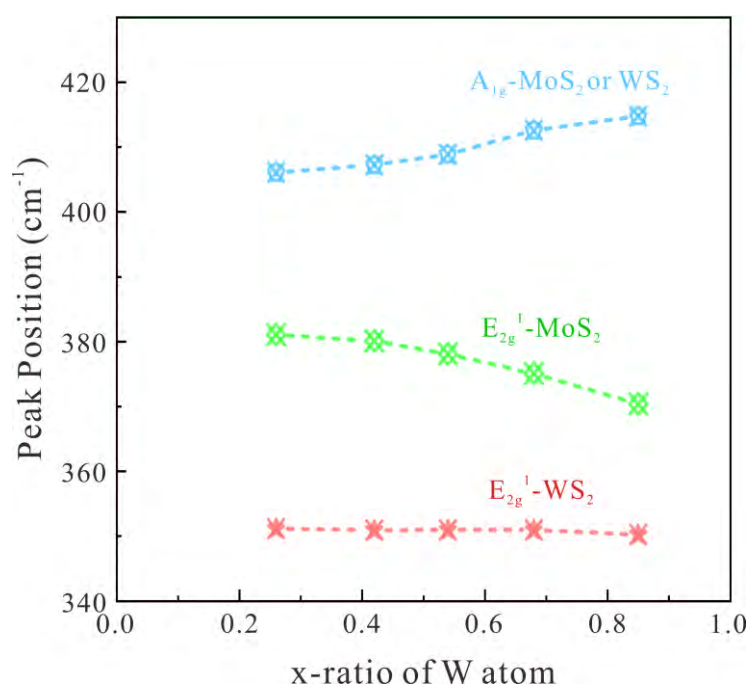


**Figure S7.** Raman peak positions of the monolayer Mo<sub>1-x</sub>W<sub>x</sub>S<sub>2</sub> alloys.

## Raman mapping

Raman mapping was conducted for the three characteristic modes of the monolayer Mo<sub>1-x</sub>W<sub>x</sub>S<sub>2</sub> ( $x = 0.54$ ) alloy, including the  $E_{2g}^1$ -WS<sub>2</sub>,  $E_{2g}^1$ -MoS<sub>2</sub>, and  $A_{1g}$  modes as shown in Figure S8. The uniform color in the images reveals the uniformity of the monolayer alloy.

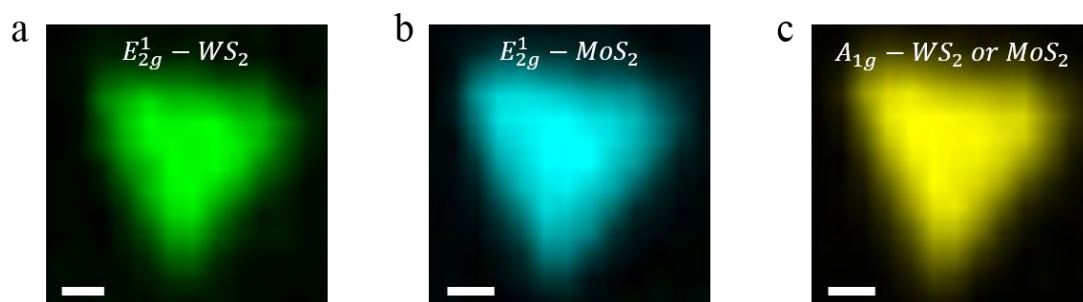


**Figure S8.** Raman maps of the monolayer  $\text{Mo}_{1-x}\text{W}_x\text{S}_2$  ( $x = 0.54$ ) alloy: (a)  $E_{2g}^1$ - $\text{WS}_2$ , (b)  $E_{2g}^1$ - $\text{MoS}_2$ , and (c)  $A_{1g}$  (Scale bar:  $1\ \mu\text{m}$ ).

### **Tunable bandgap of $\text{Mo}_{1-x}\text{W}_x\text{S}_2$ with different compositions**

The bandgap of monolayer  $\text{Mo}_{1-x}\text{W}_x\text{S}_2$  can be tuned in a wide range from 1.80 eV to 1.98 eV by adjusting the W concentration.

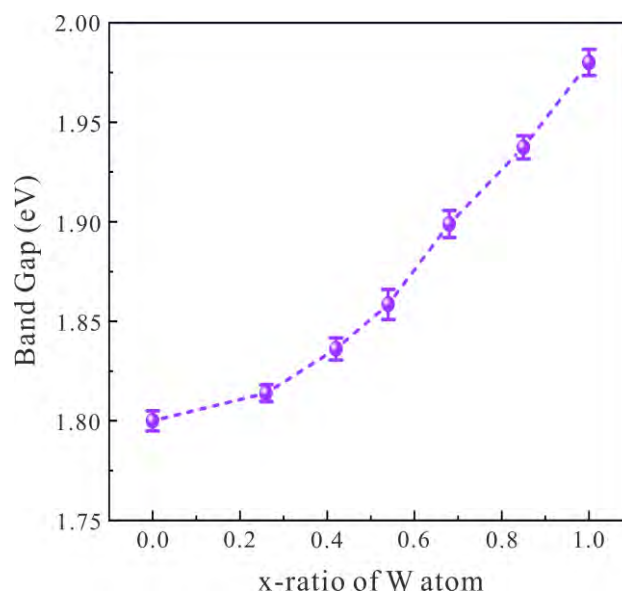


**Figure S9.** Bandgaps of the monolayer  $\text{Mo}_{1-x}\text{W}_x\text{S}_2$  samples with different compositions.

## DFT calculation

Firstly, a DFT model is built based on the lowest-energy structure at the temperature of 0 K and no entropy is taken into account (named entropy-unrelated DFT model). Disordered structures of  $\text{Mo}_{1-x}\text{W}_x\text{S}_2$  ( $x \neq 0,1$ ) are sampled by electrostatic potential method (supercell program). The identified lower-energy structures are further relaxed by DFT calculations to determine the lowest-energy structure. According to all these relaxed structures of  $\text{Mo}_{1-x}\text{W}_x\text{S}_2$ , we further carried out calculation of piezoelectric constant at 0 K ( $d_{11}^0$ ) as shown in **Table S1**. However, this entropy-unrelated calculation needs to be improved for the cationic-disordered  $\text{Mo}_{1-x}\text{W}_x\text{S}_2$  alloys in which the contribution of configurational entropy dominates.

**Table S1.** Piezoelectric properties of  $\text{Mo}_{1-x}\text{W}_x\text{S}_2$  with different x-ratio of W.

| Material-type                                       | $c_{11}$ (N/m) | $c_{12}$ (N/m) | $\epsilon_{11}$ ( $10^{-10}$ C/m) | $d_{11}^0$ (pm/V) | gap (eV) |
|---|----------------|----------------|-----------------------------------|-------------------|----------|
| MoS <sub>2</sub>                                    | 162.71         | 56.80          | 3.67                              | 3.47              | 1.78     |
| Mo <sub>0.74</sub> W <sub>0.26</sub> S <sub>2</sub> | 167.88         | 58.91          | 3.3                               | 3.02              | 1.78     |
| Mo <sub>0.58</sub> W <sub>0.42</sub> S <sub>2</sub> | 171.66         | 60.50          | 3.01                              | 2.71              | 1.80     |
| Mo <sub>0.46</sub> W <sub>0.54</sub> S <sub>2</sub> | 173.87         | 61.57          | 2.89                              | 2.57              | 1.82     |
| Mo <sub>0.32</sub> W <sub>0.68</sub> S <sub>2</sub> | 176.99         | 62.77          | 2.72                              | 2.38              | 1.85     |
| Mo <sub>0.15</sub> W <sub>0.85</sub> S <sub>2</sub> | 179.41         | 64.19          | 2.46                              | 2.14              | 1.89     |
| WS <sub>2</sub>                                     | 179.01         | 63.31          | 2.34                              | 2.02              | 1.88     |

Secondly, we rebuild an entropy-related DFT model to calculate entropy-induced

piezoelectric constants ( $d_{11}^S$ ). In our model, ambient piezoelectric constant, configurational entropy, and temperature are considered into DFT-calculated enthalpy to make second-order derivative, as following

$$G_f(298\text{K}, 1\text{atm}) = H(0\text{ K}, 1\text{atm}) - S^{\text{conf}}\Delta T(0-298\text{ K}, 1\text{atm})$$

$$\tilde{e}_{\alpha j} = -\frac{\partial^2 G}{\partial \varepsilon_{\alpha} \partial \eta_j} \Big|_u$$

In our case, only configurational entropy ( $S^{\text{conf}}$ ) is considered due to cationic disorder, i.e.,  $W^{4+}$  and  $Mo^{4+}$  and other entropy contributions could be neglected in comparison with configuration entropy. In a fixed atomic position ( $\mu$ ), on the direction of electrical quantity ( $\alpha$ ) and the direction of the mechanical quantity ( $j$ ), the piezoelectric tensor ( $\tilde{e}_{\alpha j}$ ) can be calculated by making second-order derivative of lattice change. In case of the  $Mo_{1-x}W_xS_2$  alloy system, the configurational entropy ( $S_m$ ) can be calculated using the following formula:

$$S_m = -R\left[\left(\sum_{a=1}^n x_a \ln x_a\right)_{Mo\text{-site}} + \left(\sum_{b=1}^n x_b \ln x_b\right)_{W\text{-site}} + \left(\sum_{c=1}^n x_c \ln x_c\right)_{S\text{-site}}\right]$$

where  $x_a$ ,  $x_b$  and  $x_c$  are the mole fraction of the ions present in the Mo-site, W-site and S-site, respectively.

The  $d_{11}^S$  can be calculated by comparing experimental (298 K) and DFT-calculated (0 K) piezoelectric constants. As shown in Figure S10 (a),  $Mo_{0.46}W_{0.54}S_2$  exhibits the largest entropy-induced piezoelectric constant. In whole,  $d_{11}^S$  of different species are gradually increased with configurational entropies (Figure S10 (b)). As a result, a comparative study between ambient experiments and 0 K DFT calculations reveals that  $d_{11}^S$  is significantly increased with the configurational entropy. In the  $Mo_{0.46}W_{0.54}S_2$

alloy, piezoelectric effect induced by configurational entropy occupies a large percentage due to a large configurational distribution.

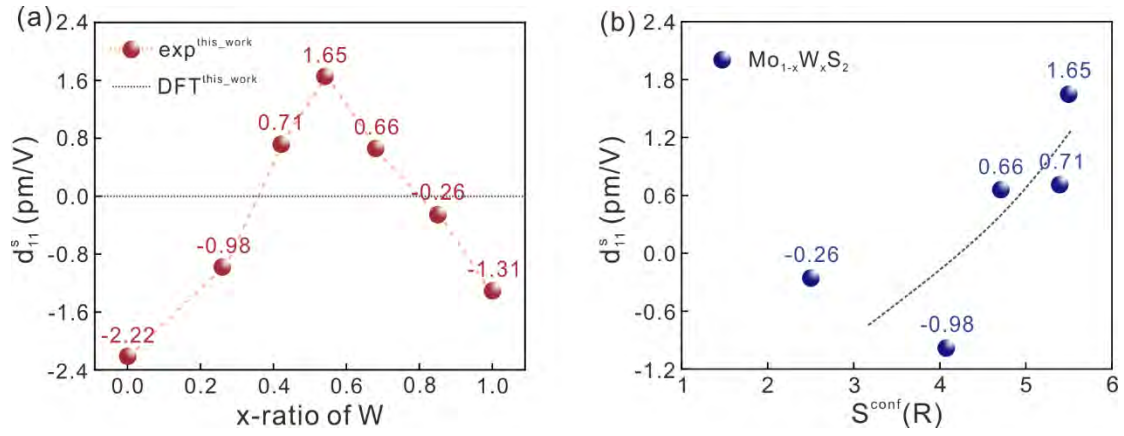


**Figure S10.** (a) DFT calculation of entropy-induced piezoelectric constants ( $d_{11}^S$ ) as a function of W fraction in  $\text{Mo}_{1-x}\text{W}_x\text{S}_2$  alloy. (b) The entropy-induced piezoelectric constants ( $d_{11}^S$ ) as a function of configurational entropy ( $S^{\text{conf}}$ ).

### **Influence of entropy on the piezoelectric output current**

The relationship between the output currents and stoichiometry is exhibited in Figure S11. All the results are obtained at a fixed strain (0.48%) and strain velocity ( $10 \text{ mm s}^{-1}$ ), and all the devices consist of triangular alloys with a size of approximately  $15 \mu\text{m}$ . The output currents of the monolayer  $\text{Mo}_{1-x}\text{W}_x\text{S}_2$  increase from  $x = 0$  to  $x = 0.54$  and then decrease from  $x = 0.54$  to  $x = 1$ . The Mo concentration is almost the same as that of W in  $\text{Mo}_{0.46}\text{W}_{0.54}\text{S}_2$  and the corresponding configurational entropy is maximized



to obtain the maximum piezoelectric output current.

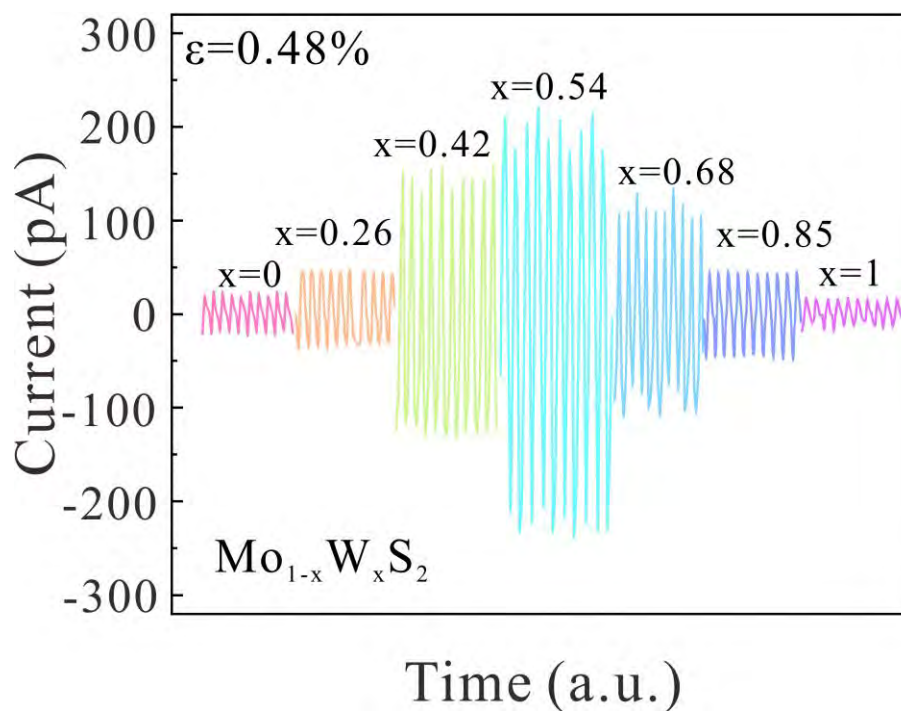


**Figure S11.** Output currents of the monolayer  $\text{Mo}_{1-x}\text{W}_x\text{S}_2$  with different W concentrations at strain of 0.48% and velocity of  $10 \text{ mm s}^{-1}$ .

### **PFM characterization**

The monolayer  $\text{Mo}_{1-x}\text{W}_x\text{S}_2$  alloys were transferred to a substrate with a two-layered structure containing a silicon wafer on the bottom and Au layer with a thickness of 50 nm on top. A gold layer was deposited by electron beam evaporation on the  $n^{++}$  silicon substrate to serve as the bottom electrode and rule out the possibility of elastic and electrostatic forces contributing to the measured electromechanical response.<sup>10</sup> Since deformation of the cantilever can cause deflection of the reflected beam, the position of the reflected light on the PSPD (position sensitive photodiode) can change and an electrical signal will be generated to reflect deformation of the cantilever. This is

employed to achieve telescopic control of the piezoelectric scanner.

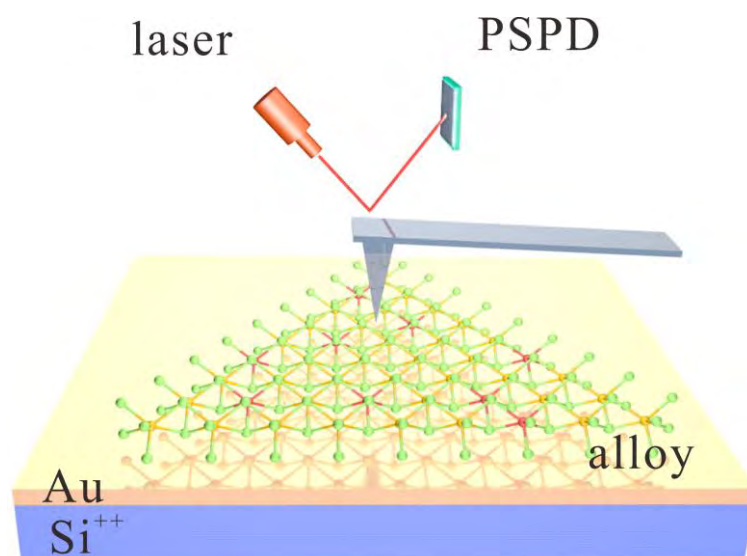


**Figure S12.** Schematic diagram of the monolayer  $\text{Mo}_{1-x}\text{W}_x\text{S}_2$  transferred to the 50 nm Au/ $\text{n}^{++}$  Si substrate for PFM characterization.

### **Substrate roughness**

To exclude the surface corrugation-mediated flexoelectricity,<sup>11</sup> the surface of the substrate for the PFM measurement should be flat. The surface roughness of the  $\text{n}^{++}$  silicon substrate depends on the deposition rate of Au. When the deposition rate of Au increases from 1 to 5  $\text{\AA s}^{-1}$ , the surface roughness increases from 0.78 to 1.32 nm accordingly. Therefore, the deposition is kept as low as possible (1  $\text{\AA s}^{-1}$ ) to obtain Au

film prior to the PFM measurement.

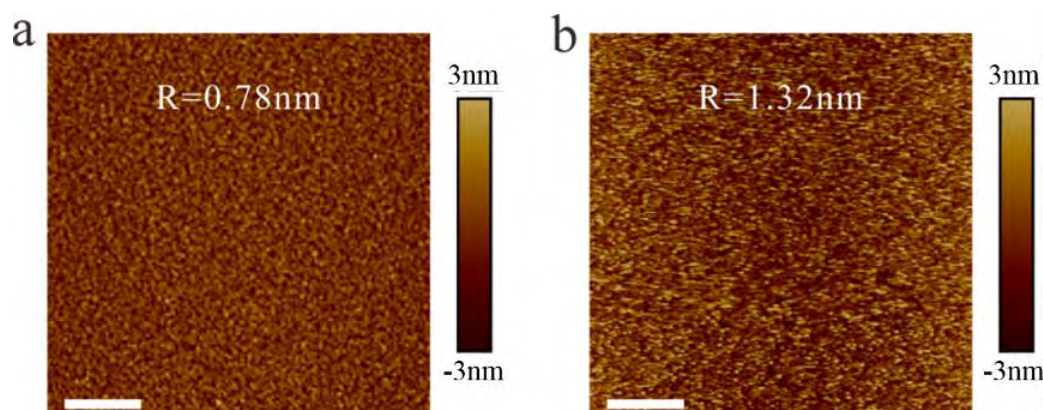


**Figure S13.** Surface roughness after Au deposition at different deposition rates: (a)  $1 \text{ \AA s}^{-1}$  and (b)  $5 \text{ \AA s}^{-1}$  (Scale bar:  $1 \text{ \mu m}$ ).

#### **PFM characterization of $\text{Mo}_{1-x}\text{W}_x\text{S}_2$ alloys:**

Figures S14-20 present the PFM amplitude and phase images of the monolayer  $\text{Mo}_{1-x}\text{W}_x\text{S}_2$  under driving voltages of 0.5, 1.0, and 1.5 V, respectively. The piezoresponse map shows that noise with a sub-picometer magnitude can be detected on Au substrate and clear borders are observed from the triangles due to onset of sliding friction.<sup>12</sup> The obvious amplitude distinction appears when the AC voltage is varied from 0.5 V to 1.5 V. The piezoresponse amplitude increases steadily in the monolayer alloy region with increasing bias and the effective piezoresponse amplitude is the difference between the materials amplitude and substrate amplitude. For instance, the piezoresponse statistics illustrates an effective piezoresponse from the monolayer  $\text{Mo}_{0.46}\text{W}_{0.54}\text{S}_2$  alloy ( $x = 0.54$ ) areas of about  $3.89 \pm 0.32 \text{ pm}$  at 0.5 V,  $5.94 \pm 0.51 \text{ pm}$  at 1.0 V AC voltage, and  $8.06 \pm 0.44 \text{ pm}$  at 1.5 V, respectively. The PFM phase signal

appears spontaneously and that of  $\pm 90^\circ$  represents the antiparallel polarization in the piezoresponse direction. Similarly, when the modulation voltage is changed from 0.5 to 1.5 V, the uniform phase response in the monolayer alloy region shows the existence of out-of-plane electromechanical coupling in a unified polarization direction.<sup>13</sup>

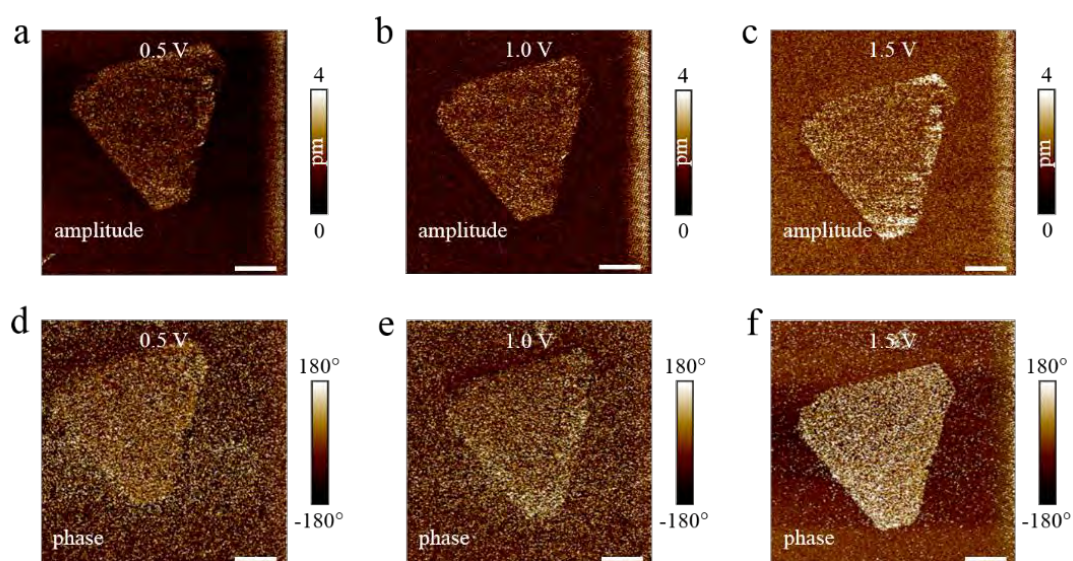


**Figure S14.** Out-of-plane piezoresponse amplitude and phase images of the monolayer MoS<sub>2</sub> at different AC voltages: (a, d) 0.5 V, (b, e) 1.0 V, and (c, f) 1.5 V (Scale bar: 2 μm).

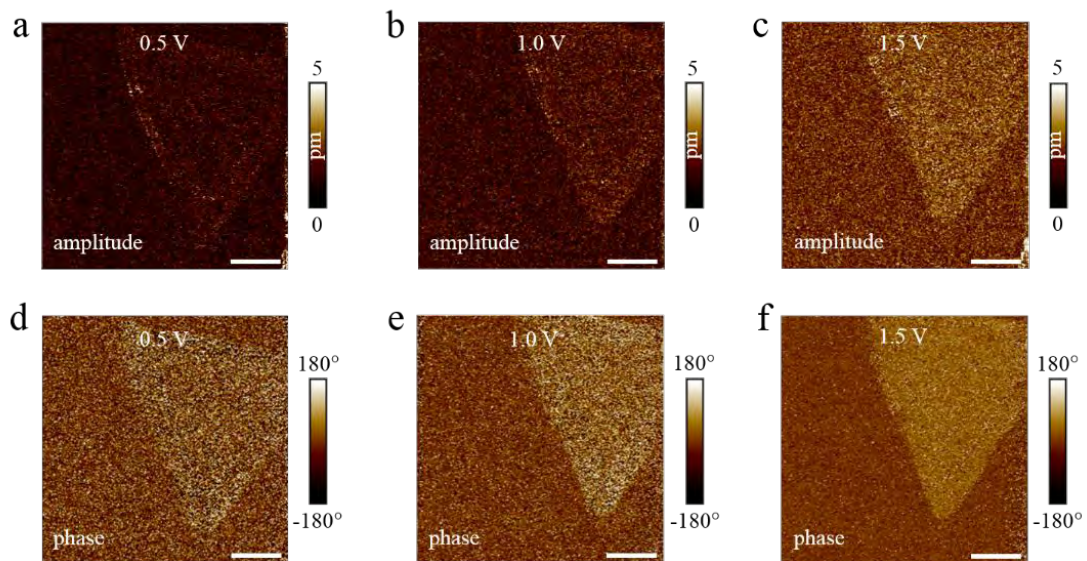


**Figure S15.** Out-of-plane piezoresponse amplitude and phase images of the monolayer  $\text{Mo}_{0.74}\text{W}_{0.26}\text{S}_2$  at different AC voltages: (a, d) 0.5 V, (b, e) 1.0 V, and (c, f) 1.5 V (Scale bar: 1  $\mu\text{m}$ ).

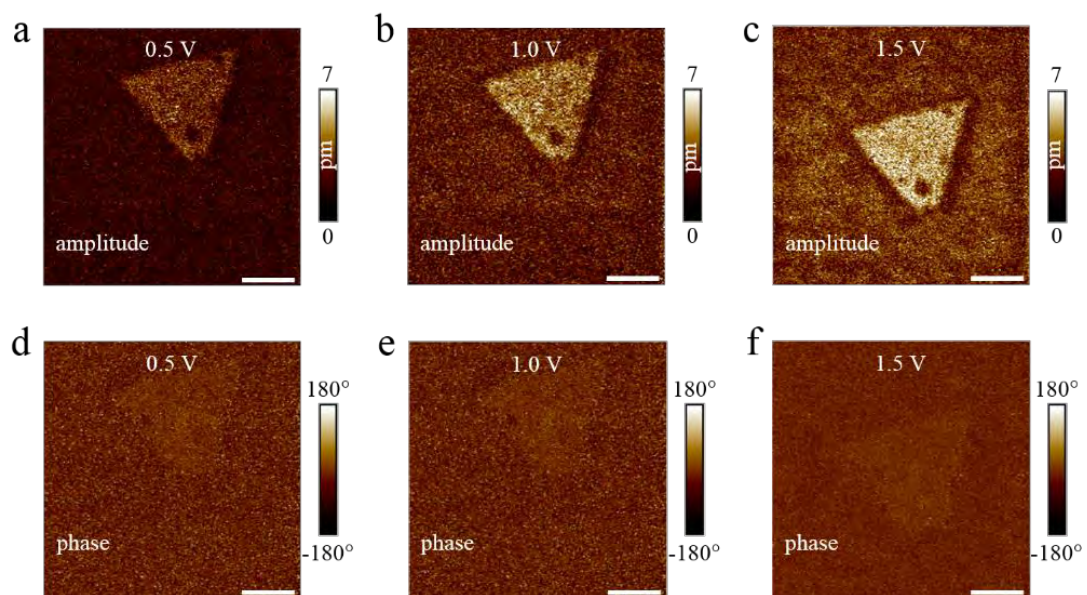


**Figure S16.** Out-of-plane piezoresponse amplitude and phase images of the monolayer  $\text{Mo}_{0.58}\text{W}_{0.42}\text{S}_2$  at different AC voltages: (a, d) 0.5 V, (b, e) 1.0 V, and (c, f) 1.5 V (Scale bar: 2  $\mu\text{m}$ ).

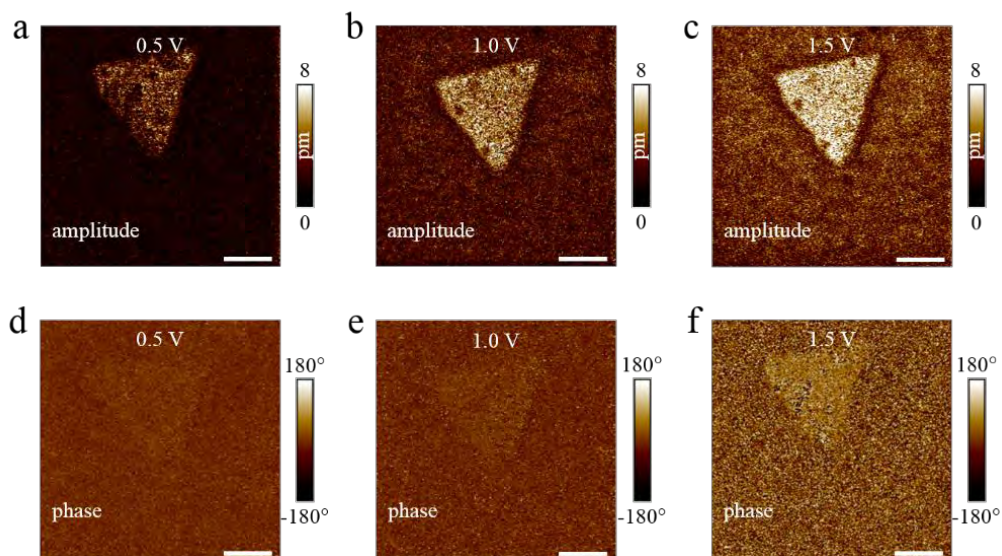


**Figure S17.** Out-of-plane piezoresponse amplitude and phase images of monolayer  $\text{Mo}_{0.46}\text{W}_{0.54}\text{S}_2$  at different AC voltages: (a, d) 0.5 V, (b, e) 1.0 V, and (c, f) 1.5 V (Scale bar: 2  $\mu\text{m}$ ).

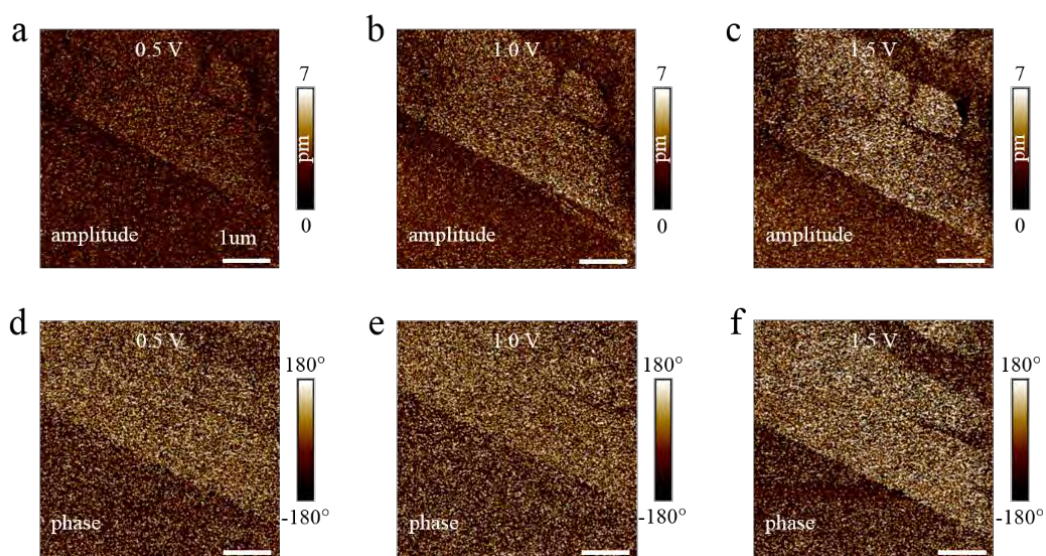


**Figure S18.** Out-of-plane piezoresponse amplitude and phase images of monolayer  $\text{Mo}_{0.32}\text{W}_{0.68}\text{S}_2$  at different AC voltages: (a, d) 0.5 V, (b, e) 1.0 V, and (c, f) 1.5 V (Scale bar: 1  $\mu\text{m}$ ).

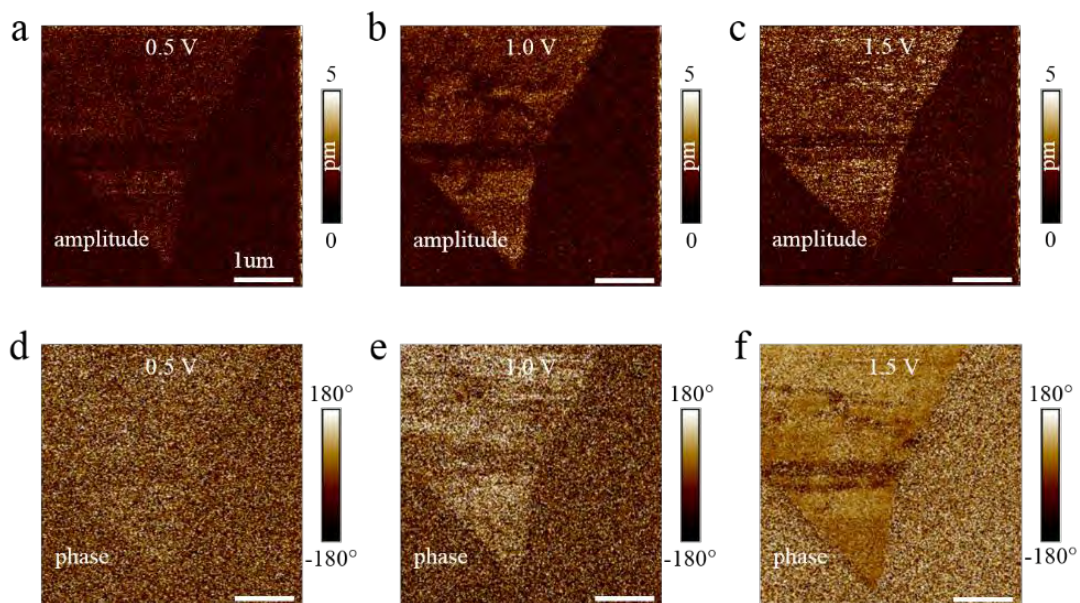


**Figure S19.** Out-of-plane piezoresponse amplitude and phase images of monolayer  $\text{Mo}_{0.15}\text{W}_{0.85}\text{S}_2$  at different AC voltages: (a, d) 0.5 V, (b, e) 1.0 V, and (c, f) 1.5 V (Scale bar: 1  $\mu\text{m}$ ).

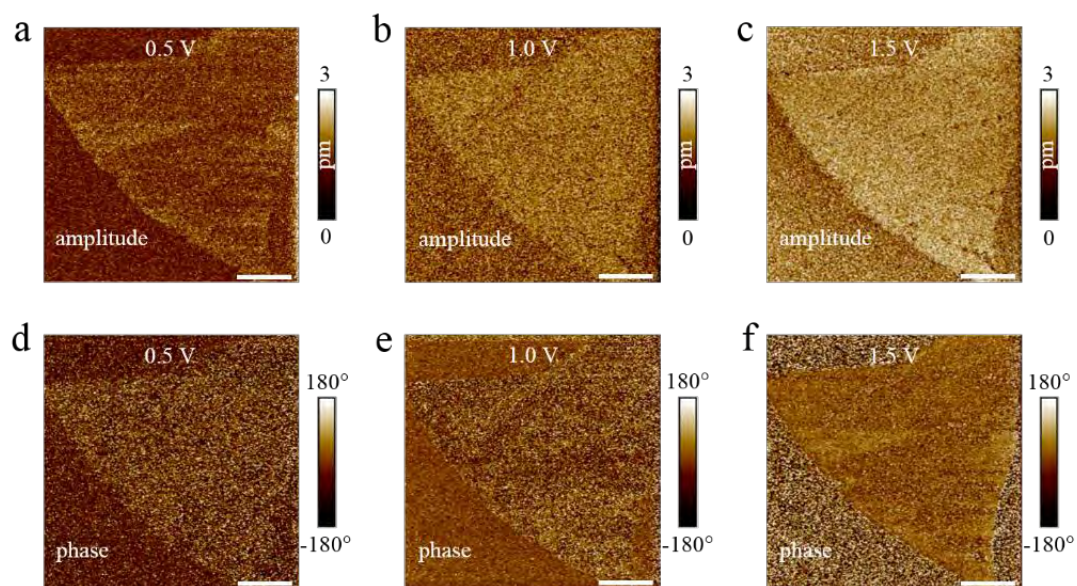


**Figure S20.** Out-of-plane piezoresponse amplitude and phase images of monolayer  $\text{WS}_2$  at different AC voltages: (a, d) 0.5 V, (b, e) 1.0 V, and (c, f) 1.5 V (Scale bar: 1  $\mu\text{m}$ ).

### **Fabrication details:**

To fabricate the nanogenerator device, the PET substrate with a thickness of 188  $\mu\text{m}$  was used. Unlike the traditional  $\text{SiO}_2/\text{Si}$  substrate, the monolayer alloys were too thin to be put on a transparent PET substrate and it was necessary to mark the PET substrate. The Au marks on the PET film were patterned by photolithography and the unnecessary areas were lifted off with the NMP (N-methylpyrrolidone) solution as shown in Figures S21 (a) and (b). In the process, 10B was spin-coated onto the PET substrate at 4000 rpm and annealed at  $150^\circ\text{C}$ . Afterwards, AZ5214 was spin-coated on the 10B/PET substrate at 4000 rpm, and annealed at  $100^\circ\text{C}$  to avoid the possible deformation occurring at high annealing temperature, since the deform would severely thus affect the lithographic accuracy. Finally, the micrometer-scale monolayer  $\text{Mo}_{0.46}\text{W}_{0.54}\text{S}_2$  alloy was transferred to the Au marked PET substrate by a PVA-assisted method as illustrated in Figure S21 (c).



**Figure S21.** Optical images: (a) Marked PET substrate, (b) Magnified image of the dashed yellow area in (a) (Scale bar:  $200\ \mu\text{m}$ ), and (c) Transferred monolayer  $\text{Mo}_{0.46}\text{W}_{0.54}\text{S}_2$  alloy on PET substrate (Scale bar:  $40\ \mu\text{m}$ ).



### Output voltages of IE-PNG

At the strain of 0.48% and the strain rate of 10 mm/s, the output voltages of the piezoelectric nanogenerator based on  $\text{Mo}_{0.46}\text{W}_{0.54}\text{S}_2$  with increased entropy (IE-PNG) under different load resistances are collected, as shown in Figure S22 (a). For the load resistance increase from 10 to 1000  $\text{M}\Omega$ , the output signal increases from 6 to 42 mV accordingly. Figure S22 (b) shows the output performance of  $\text{Mo}_{0.46}\text{W}_{0.54}\text{S}_2$  devices as a function of strain rate at the fixed strain of 0.48%. As the strain rate increases from 2.5 to 10 mm/s, the voltage increases from 11 to 40 mV accordingly.

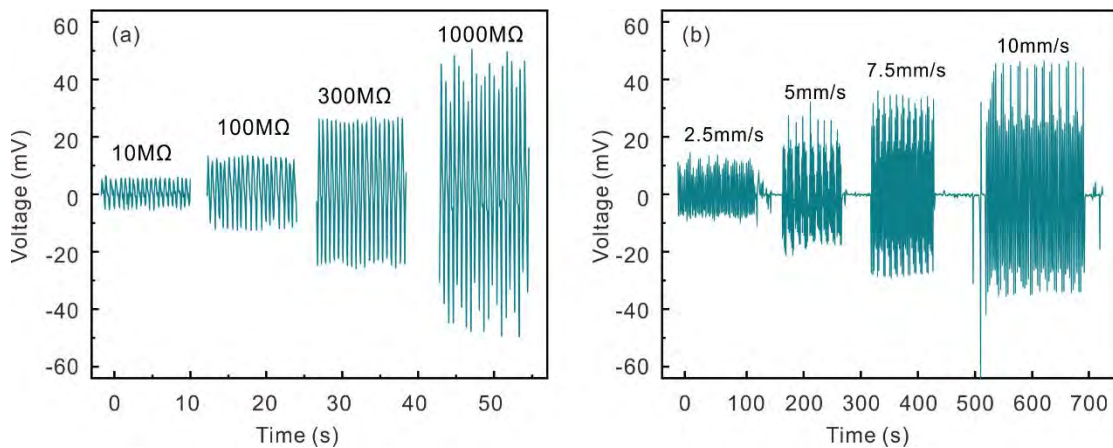


**Figure S22.** The output voltages of the piezoelectric nanogenerator based on  $\text{Mo}_{0.46}\text{W}_{0.54}\text{S}_2$  with increased entropy (IE-PNG) under different load resistances (a) and different strain rates (b).

## Layer-dependent output current

In pure component 2D material case, two-layer 2H-MoS<sub>2</sub> membranes do not possess piezoelectricity due to a symmetric cancellation of alternating orientations between the adjacent layers, as shown in Figure S23 (a). As a result, piezoelectric signal disappears in two-layer 2H-stacked MoS<sub>2</sub> without breaking inversion symmetry. In our case, the disordered doping of Mo<sub>1-x</sub>W<sub>x</sub>S<sub>2</sub> will introduce the inherent asymmetry character in atomic structures, which is able to avoid the complete cancellation from two neighboring layers observed in two-layer 2H-stacked MoS<sub>2</sub> (shown in Figure S23 (b)). We also measure the piezoelectric property of two-layer Mo<sub>0.46</sub>W<sub>0.54</sub>S<sub>2</sub>. It is found that the piezoelectric output current is significantly degraded for two-layer Mo<sub>0.46</sub>W<sub>0.54</sub>S<sub>2</sub> compared to mono-layer Mo<sub>0.46</sub>W<sub>0.54</sub>S<sub>2</sub>, but it really exists due to the incomplete cancellation from two neighboring layers, as shown in Figure S23 (c). The piezoelectric output current of the mono-layer Mo<sub>0.46</sub>W<sub>0.54</sub>S<sub>2</sub> is ~200 pA, while it is ~40 times larger than that of two-layer Mo<sub>0.46</sub>W<sub>0.54</sub>S<sub>2</sub> (5 pA).

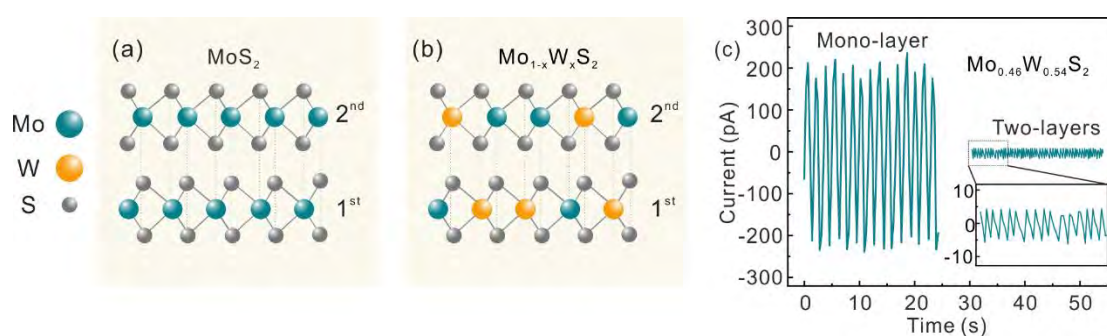


**Figure S23.** Structure of repeating two-layer units in 2H-stacked (a) MoS<sub>2</sub> and (b) Mo<sub>1-x</sub>W<sub>x</sub>S<sub>2</sub>. (c) Piezoelectric output currents of Mo<sub>0.46</sub>W<sub>0.54</sub>S<sub>2</sub> with different atomic layers.

### Output currents at larger strain

When the strain is increased to 0.96%, the metal and monolayer materials slip in turn producing discontinuous electrical signals as shown in Figure S24.

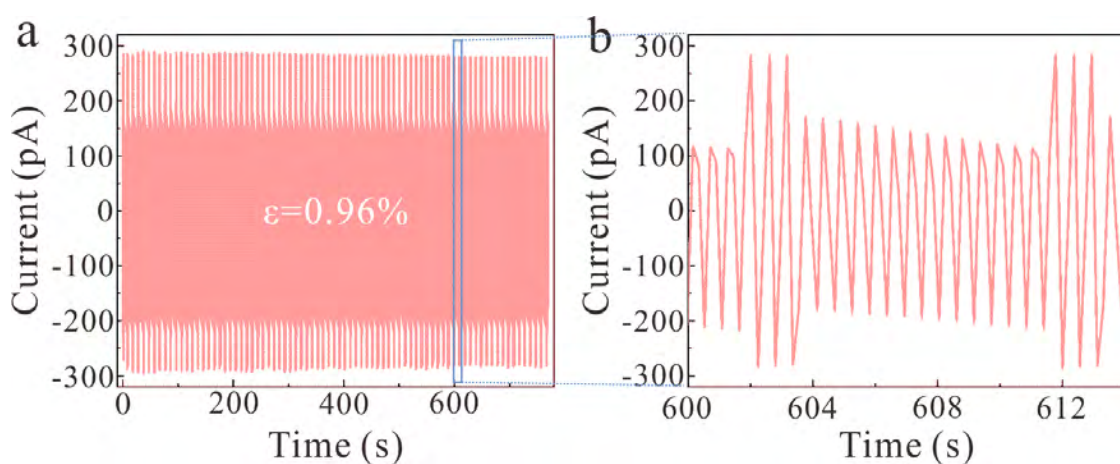


**Figure S24.** (a) Mechanical durability test of the output current of  $\text{Mo}_{0.46}\text{W}_{0.54}\text{S}_2$  PNG under continuous cyclic compressive strain of 0.96% and (b) Magnified image of the blue area in (a).

### Mechanical stability of nanogenerators:

The nanogenerators can operate under continuous application of cyclic compressive force for low strain of 0.24% and 0.48% (Figure S25). Energy conversion is stable for long cyclic time confirming the good mechanical durability of the nanogenerators.

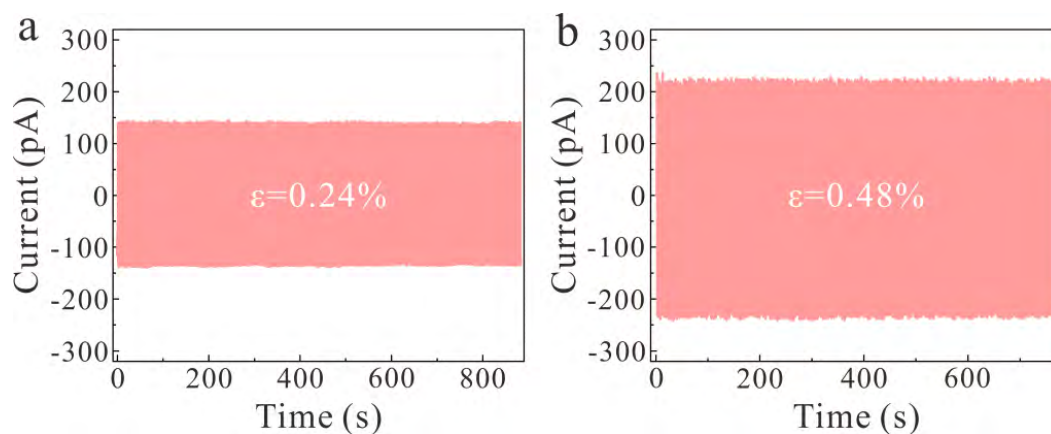


**Figure S25.** Mechanical durability test of the output currents of the Mo<sub>0.46</sub>W<sub>0.54</sub>S<sub>2</sub> PNG under continuous application of cyclic compressive strain of (a) 0.24% and (b) 0.48%.

## References

1. A. M. van der Zande, P. Y. Huang, D. A. Chenet, T. C. Berkelbach, Y. You, G. H. Lee, T. F. Heinz, D. R. Reichman, D. A. Muller, J. C. Hone, *Nature Mater.* **2013**, 12, 554.
2. Q. Huang, X. Li, M. Sun, L. Zhang, C. Song, L. Zhu, P. Chen, Z. Xu, W. Wang, X. Bai, *Adv. Mater. Interfaces*, **2017**, 4, 1700171.
3. L. Yang, X. Cui, J. Zhang, K. Wang, M. Shen, S. Zeng, S. A. Dayeh, L. Feng, B. Xiang, *Sci. rep.* **2014**, 4, 1.
4. X. Wang, H. Feng, Y. Wu, L. Jiao, *JACS*, **2013**, 135, 5304.
5. S. Cravanzola, L. Muscuso, F. Cesano, G. Agostini, A. Damin, D. Scarano, A. Zecchina, *Langmuir* **2015**, 31, 5469.
6. V. O. Koroteev, L. G. Bulusheva, A. V. Okotrub, N. F. Yudanov, D. V. Vyalikh, *Phys. Status Solidi B* **2011**, 248, 2740.

7. A. Cordova, P. Blanchard, H. Salembier, C. Lancelot, G. Frémy, C. Lamonier, *Catal. Today* **2017**, 292, 143.
8. A. Cordova, P. Blanchard, C. Lancelot, G. Frémy, C. Lamonier, *ACS Catal.* **2015**, 5, 2966.
9. L. Liu, J. Wu, L. Wu, M. Ye, X. Liu, Q. Wang, S. Hou, P. Lu, L. Sun, J. Zheng, L. Xing, L. Gu, X. Jiang, L. Xie, L. Jiao, *Nature Mater.* **2018**, 17, 1108.
10. C. J. Brennan, R. Ghosh, K. Koul, S. K. Banerjee, N. Lu, E. T. Yu, *Nano Lett.* **2017**, 17, 5464.
11. S. Kang, S. Jeon, S. Kim, D. Seol, H. Yang, J. Lee, Y. Kim, *ACS Appl Mater Interfaces* **2018**, 10, 27424.
12. S. Jesse, A. P. Baddorf, S. V. Kalinin, *Nanotechnology* **2006**, 17, 1615.
13. D. Zhang, Z. Yang, P. Li, M. Pang, Q. Xue, *Nano Energy* **2019**, 65, 103974.